Monthly Notices
of the
ROYAL ASTRONOMICAL SOCIETY

MNRAS **447,** 3973–3991 (2015) doi:10.1093/mnras/stu2637

The UK Infrared Telescope M33 monitoring project – IV. Variable red giant stars across the galactic disc

Atefeh Javadi,[1]★ Maryam Saberi,[3] Jacco Th. van Loon,[2] Habib Khosroshahi,[1] Najmeh Golabatooni[3] and Mohammad Taghi Mirtorabi[3]

[1]*School of Astronomy, Institute for Research in Fundamental Sciences (IPM), PO Box 19395-5531 Tehran, Iran*
[2]*Astrophysics Group, Lennard-Jones Laboratories, Keele University, Staffordshire ST5 5BG, UK*
[3]*Physics Department, Alzahra University, Vanak, 1993891176 Tehran, Iran*

Accepted 2014 December 10. Received 2014 December 10; in original form 2014 September 15

ABSTRACT

We have conducted a near-infrared monitoring campaign at the UK InfraRed Telescope, of the Local Group spiral galaxy M33 (Triangulum). The main aim was to identify stars in the very final stage of their evolution, and for which the luminosity is more directly related to the birth mass than the more numerous less-evolved giant stars that continue to increase in luminosity. In this fourth paper of the series, we present a search for variable red giant stars in an almost square degree region comprising most of the galaxy's disc, carried out with the WFCAM (Wide Field CAMera) instrument in the *K* band. These data, taken during the period 2005–2007, were complemented by *J*- and *H*-band images. Photometry was obtained for 403 734 stars in this region; of these, 4643 stars were found to be variable, most of which are asymptotic giant branch (AGB) stars. The variable stars are concentrated towards the centre of M33, more so than low-mass, less-evolved red giants. Our data were matched to optical catalogues of variable stars and carbon stars and to mid-infrared photometry from the *Spitzer* Space Telescope. Most dusty AGB stars had not been previously identified in optical variability surveys, and our survey is also more complete for these types of stars than the *Spitzer* survey. The photometric catalogue is made publicly available at the Centre de Données astronomiques de Strasbourg.

Key words: stars: evolution – stars: luminosity function, mass function – stars: mass-loss – stars: oscillations – galaxies: individual: M33 – galaxies: stellar content.

1 INTRODUCTION

The Local Group galaxy Triangulum (Hodierna 1654) – hereafter referred to as M33 (Messier 1771) – offers us a unique opportunity to study stellar populations, their history, and their feedback across an entire spiral galaxy and in particular in its central regions, that in our own Milky Way are heavily obscured by the intervening dusty disc (van Loon et al. 2003; Benjamin et al. 2005). Our viewing angle with respect to the M33 disc is more favourable (56°–57° – Deul & van der Hulst 1987; Zaritsky, Elston & Hill 1989) than that of the larger M 31 (Andromeda), whilst the distance to M33 is not much different from that to M 31 ($\mu = 24.9$ mag – Bonanos et al. 2006). For these reasons, numerous surveys have been conducted to study M33 in different wavelength ranges including optical (Macri et al. 2001; Hartman et al. 2006; Massey et al. 2006); radio (Engargiola et al. 2003); X-ray (Pietsch et al. 2004); and infrared (IR – Two Micron All Sky Survey [2MASS]; Skrutskie et al. 2006; McQuinn et al. 2007). Large populations of asymptotic giant branch (AGB) stars have been identified in M33 (Cioni et al. 2008), as well as red supergiants (RSGs) up to progenitor masses in excess of 20 $M_\odot$ (Drout, Massey & Meynet 2012). Many of them are dusty long period variables (LPVs – McQuinn et al. 2007; Thompson et al. 2009), and these have been found also in the central parts of M33 (Javadi, van Loon & Mirtorabi 2011a; Javadi et al. 2013).

In the final stage of stellar evolution, low–medium mass (0.8–8 $M_\odot$) stars enter the AGB phase (Marigo et al. 2008) and more massive stars ($M > 8$ $M_\odot$) enter the RSG phase (Levesque et al. 2005; Levesque 2010). These two phases of evolution trace stellar populations over a range in age from ∼10 Myr to ∼10 Gyr, and hence the evolution of their host galaxies over essential all cosmological time. Radial pulsations of the atmospheric layers in AGB stars and RSGs yield long-period variability of the order of 150–1500 d in the photometric light curves (e.g. Wood et al. 1992; Wood 1998; Pierce, Jurcević & Crabtree 2000; Whitelock et al. 2003). Most-evolved AGB stars pulsate in the fundamental mode,

★ E-mail: atefeh@ipm.ir

while less-evolved AGB stars and RSGs pulsate in an overtone; as a result, the amplitude of variability expressed in magnitude of AGB stars are larger than that of RSGs and less-evolved AGB stars. These LPVs are powerful tools to study the star formation history of galaxies, and to this aim various variability surveys have been conducted of M33 over recent years (Macri et al. 2001; Mochejska et al. 2001a,b; Hartman et al. 2006; Sarajedini et al. 2006; McQuinn et al. 2007).

The coolest ($T \sim$ 3000–4000 K) and most luminous (∼10 000–60 000 $L_{\odot}$) AGB stars create large amounts of dust in the stars atmosphere. This dust is ejected into space and can cloak the star, especially in the optical light, and add luminosity at IR wavelengths. Likewise, RSGs stand out especially at IR wavelengths. Hence, among all surveys, those with the *Spitzer* Space Telescope (McQuinn et al. 2007) and the UK InfraRed Telescope (UKIRT; Javadi et al. 2011a) were more successful in detecting dusty LPVs. Since these evolved stars shed a large amount of mass into the interstellar medium (ISM), they are important factors in changing the chemical composition of galaxies and incrementing the rate of stellar birth.

The main objectives of our project are described in Javadi, van Loon & Mirtorabi (2011c): to construct the mass function of LPVs and derive from this the star formation history in M33; to correlate spatial distributions of the LPVs of different mass with galactic structures (spheroid, disc, and spiral arm components); to measure the rate at which dust is produced and fed into the ISM; to establish correlations between the dust production rate, luminosity, and amplitude of an LPV; and to compare the *in situ* dust replenishment with the amount of pre-existing dust. Paper I in the series presented the photometric catalogue of stars in the inner square kpc (Javadi et al. 2011a), with Paper II presenting the galactic structure and star formation history (Javadi, van Loon & Mirtorabi 2011b), and Paper III presenting the mass-loss mechanism and dust production rate (Javadi et al. 2013). This paper describes the extension of the survey to a nearly square degree area covering much of the M33 optical disc. Subsequent papers in the series will cover the star formation history and mass return in this enlarged area.

In Section 2, we present the observational data, method of photometry on the images, and accuracy of these measurements. The methodology and completeness of our search for LPVs, and characterization of their amplitude of variability are discussed in Section 3. Section 4 describes the photometric catalogue of all detected stars, which is made available at the Centre de Données astronomiques de Strasbourg (CDS). In Section 5, we describe the properties and distribution of the detected LPVs and also compare these with other (optical and IR) variability surveys and stellar catalogues. Section 6 summarizes and concludes the results.

2 OBSERVATIONS

Observations were made with three of UKIRT's imagers: UIST, UFTI, and Wide Field CAMera (WFCAM). UIST and UFTI cover the central part (≈1 kpc^2) and the photometry, star formation history, and mass return in this region was explained in Papers I, II, and III. In this sequel, we focus on the data from WFCAM, which cover a much larger part of M33.

2.1 WFCAM

The monitoring campaign comprises observations with the WFCAM such that four separately pointed observations ('tiles', viz. M33-1, M33-2, M33-3, and M33-4) may be combined to cover a filled square area of sky covering 0.89 deg^2 (13 kpc × 13 kpc) at a pixel size of 0.″4 arcsec. The approximate centres of the camera pointings are, respectively ($1^h33^m19^s.30$, $+30^\circ32'50''$), ($1^h34^m22^s.50$, $+30^\circ32'50''$), ($1^h34^m22^s.50$, $+30^\circ46'23''$), ($1^h33^m19^s.30$, $+30^\circ46'23''$). Observations were made in the *K* band (UKIRT filter *K*98) over the period 2005 September–2007 October (Table 1). On some occasions, observations were made also in the *J* band and/or *H* band (UKIRT filters *J*98 and *H*98, respectively) to provide colour information. The total integration on one tile was achieved through four separate exposures. The number of epochs varies per tile between five and eight, but overlapping regions will have been observed more frequently.

Table 1. Log of our observations of each of four tiles ('*Q*').

Date (y m d)	*Q*	Filte\rlapr	Epoch	t_{int} (min\rlap)	Airmass
2005 09 18	3	*K*	1	\llap20.3	1.035–1.058
2005 09 18	2	*K*	1	\llap20.3	1.072–1.110
2005 09 18	4	*K*	1	\llap20.3	1.248–1.338
2005 09 19	1	*K*	1	\llap20.3	1.021–1.018
2005 10 18	3	*K*	2	\llap20.3	1.019–1.021
2005 10 18	2	*K*	2	\llap20.3	1.025–1.040
2005 10 18	4	*K*	2	\llap20.3	1.053–1.083
2005 10 18	1	*K*	2	\llap20.3	1.101–1.149
2005 11 04	1	*K*	3	\llap20.3	1.018–1.023
2005 11 04	2	*K*	3	\llap13.5	1.028–1.036
2005 12 23	2	*K*	4	\llap27.0	1.019–1.022
2005 12 23	3	*K*	3	\llap20.3	1.028–1.046
2006 07 21	1	*K*	4	\llap20.3	1.425–1.325
2006 07 21	2	*K*	5	\llap20.3	1.287–1.214
2006 07 21	3	*K*	4	\llap20.3	1.183–1.132
2006 07 21	4	*K*	3	\llap20.3	1.109–1.074
2006 10 28	1	*K*	5	\llap27.0	1.294–1.126
2006 10 28	1	*J*	1	\llap20.3	1.102–1.076
2006 10 29	1	*K*	6	\llap20.3	1.445–1.347
2006 10 29	1	*H*	1	\llap27.0	1.295–1.209
2006 10 29	1	*J*	2	\llap27.0	1.115–1.062
2006 10 30	1	*J*	2	\llap33.8	1.200–1.109
2006 10 30	4	*K*	4	\llap33.8	1.085–1.044
2006 10 31	4	*H*	1	6.8	1.301–1.301
2006 12 05	2	*K*	6	\llap20.3	1.019–1.025
2006 12 12	3	*K*	5	\llap20.3	1.082–1.052
2006 12 12	3	*H*	1	\llap20.3	1.040–1.027
2007 01 14	1	*K*	7	\llap20.3	1.124–1.169
2007 01 14	1	*J*	3	\llap20.3	1.217–1.284
2007 01 14	1	*H*	2	\llap20.3	1.342–1.441
2007 01 15	2	*K*	7	\llap20.3	1.119–1.163
2007 01 16	2	*H*	1	\llap20.3	1.063–1.092
2007 01 17	3	*J*	1	\llap20.3	1.031–1.047
2007 01 18	2	*J*	2	\llap20.3	1.029–1.044
2007 01 25	3	*K*	6	\llap20.3	1.072–1.104
2007 01 25	3	*H*	2	\llap20.3	1.161–1.215
2007 09 14	1	*K*	8	\llap20.3	1.122–1.086
2007 09 14	1	*J*	4	\llap13.5	1.070–1.058
2007 09 14	1	*H*	3	\llap13.5	1.046–1.038
2007 09 19	2	*K*	8	\llap20.3	1.774–1.606
2007 10 04	2	*J*	3	\llap13.5	1.208–1.181
2007 10 04	2	*H*	2	\llap13.5	1.155–1.132
2007 10 13	3	*K*	7	\llap20.3	1.108–1.076
2007 10 13	3	*H*	3	\llap13.5	1.056–1.046
2007 10 24	4	*K*	5	\llap20.3	1.135–1.097
2007 10 24	3	*J*	2	\llap13.5	1.078–1.064
2007 10 24	4	*J*	1	\llap13.5	1.050–1.041
2007 10 24	4	*H*	2	\llap13.5	1.025–1.022

Table 2. Log of WFCAM observations of each of four tiles ('*Q*'), from programme U/05B/7.

Date (y m d)	Q	Filte\rlapr	Epoch	t_{int} (min\rlap)	Airmass
2005 09 29	4–1	*J*	1	1.0	1.196–1.197
2005 09 29	4–1	*H*	1	4.5	1.206–1.227
2005 09 29	4–1	*K*	1	4.5	1.227–1.023
2005 09 30	2–1	*J*	1	1.0	1.023–1.023
2005 09 30	2–1	*H*	1	4.5	1.024–1.024
2005 09 30	2–1	*K*	1	4.5	1.028–1.028
2005 09 30	2–3	*J*	1	1.0	1.055–1.056
2005 09 30	2–3	*H*	1	4.5	1.060–1.060
2005 09 30	2–3	*K*	1	4.5	1.069–1.069
2005 10 24	1–1	*J*	1	1.0	1.335–1.333
2005 10 24	1–1	*H*	1	4.5	1.320–1.319
2005 10 24	1–1	*K*	1	4.5	1.293–1.292
2005 10 24	1–2	*J*	1	1.0	1.050–1.020
2005 10 24	1–2	*H*	1	4.5	1.340–1.210
2005 10 24	1–2	*K*	1	4.5	1.210–1.120
2005 10 24	1–3	*J*	1	1.0	1.204–1.202
2005 10 24	1–3	*H*	1	4.5	1.193–1.193
2005 10 24	1–3	*K*	1	4.5	1.175–1.174
2005 10 24	1–4	*J*	1	1.0	1.158–1.157
2005 10 24	1–4	*H*	1	4.5	1.145–1.144
2005 10 24	1–4	*H*	1	4.5	1.130–1.130
2005 11 05	3–1	*K*	1	4.5	1.073–1.073
2005 11 05	3–1	*H*	1	4.5	1.064–1.064
2005 11 05	3–1	*J*	1	1.0	1.055–1.055
2005 11 05	3–2	*K*	1	4.5	1.052–1.052
2005 11 05	3–2	*H*	1	4.5	1.046–1.046
2005 11 05	3–2	*J*	1	1.0	1.039–1.038
2005 11 27	1–1	*J*	2	1.0	1.292–1.295
2005 12 16	1–1	*J*	2	1.0	1.107–1.106
2005 12 16	1–1	*H*	2	4.5	1.101–1.101
2005 12 16	1–1	*K*	2	4.5	1.090–1.089
2005 12 16	1–2	*J*	2	1.0	1.079–1.078
2005 12 16	1–2	*H*	2	4.5	1.074–1.074
2005 12 16	1–2	*K*	2	4.5	1.065–1.064
2005 12 16	1–3	*J*	2	1.0	1.055–1.054
2005 12 16	1–3	*H*	2	4.5	1.051–1.051
2005 12 16	1–3	*K*	2	4.5	1.044–1.044
2005 12 16	1–4	*J*	2	1.0	1.038–1.038
2005 12 16	1–4	*H*	2	4.5	1.035–1.035
2005 12 16	1–4	*K*	2	4.5	1.031–1.031

The large pixel scale of WFCAM means that the point spread function (PSF) is not always adequately sampled for the crowded fields in M33 under modal observing conditions; to remedy this, we employed a 3 × 3 microstepping scheme to improve the sampling of the PSF. At each position of the nine-point microstepping sequence, a 5 s exposure was taken, and a small offset ('jitter', ≈05 arcsec) was applied between each of nine subsequent microstep sequences. This cycle was repeated three times. Thus, a typical observation accrued a total integration time of ≈20 min; however, in practice fewer or more repeats were performed depending on conditions, time available, or for technical reasons (interruptions).

The images were processed using the WFCAM pipeline by the Cambridge Astronomy Survey Unit (CASU – http://casu.ast.cam.ac.uk/). The main steps include:

(i) dark current correction;

(ii) flat field correction to remove pixel sensitivity differences and gain differences between data channels and between detectors;

Table 3. Log of WFCAM observations of each of four tiles ('Q'), from programme U/05B/H47.

Date (y m d)	*Q*	Filte\rlapr	Epoch	t_{int} (min\rlap)	Airmass
2005 10 20	1	*K*	1	8.3	1.077–1.059
2005 10 20	2	*K*	1	8.3	1.052–1.041
2005 10 20	3	*K*	1	8.3	1.038–1.030
2005 10 20	4	*K*	1	8.3	1.028–1.023

(iii) confidence map generation: a normalized inverse weight map denoting the confidence associated with the flux values in each pixel;

(iv) defringing, provided the fringe spatial pattern was available;

(v) sky subtraction, either using the ditter sequences themselves (our case) or using observations of offset sky regions;

(vi) image persistence and detector cross-talk correction, i.e. modelling and removing electronic effects;

(vii) combine ('interleave') the images from the microstepping sequence;

(viii) shift and average individual images from the jittering sequence;

(ix) catalogue generation. Objects are identified from the images and listed in FITS binary tables. This catalogue includes assorted aperture flux measures, intensity-weighted centroid estimates, and shape information such as intensity-weighted second moments to encode the equivalent elliptical Gaussian light distribution;

(x) astrometric calibration. All objects in the catalogue are matched to astrometric standards to define a World Coordinate System for each image/catalogue;

(xi) photometric zero-point from comparison of instrumental magnitudes with 2MASS (*K* band is K_s).

Our programme IDs are U/05B/18, U/06B/40, and U/07B/17. We have complemented our data with WFCAM archival data taken for two projects, viz. U/05B/7 and U/05B/H47 which we briefly describe below.

2.1.1 U/05B/7

The data of this programme (Cioni et al. 2008) were taken to survey the luminous red giant stars of Local Group galaxies. M33 was observed on four occasions: 2005 September 29 and 30, October 24, November 5, and December 16 (Table 2). JHK_s photometry was obtained from a mosaic of four fields (instead of the one central field in our case), covering an area ≈3 deg^2. The *H* and K_s data were acquired employing a three-point jitter pattern with 3 × 3 microstepping and 10 s exposures per position, giving a total integration time of 270 s. The *J* data were acquired using a five-point jitter pattern with three 10 s exposures but no microstepping, resulting in a total integration time of 150 s. The data were processed by the CASU.

2.1.2 U/05B/H47

The M33 data for this programme (PI: M. Irwin) were acquired on 2005 October 20 (Table 3). The covering area is nearly identical to ours, with the camera pointings called M33-position 1, M33-position 2, M33-position 3, and M33-position 4, respectively.

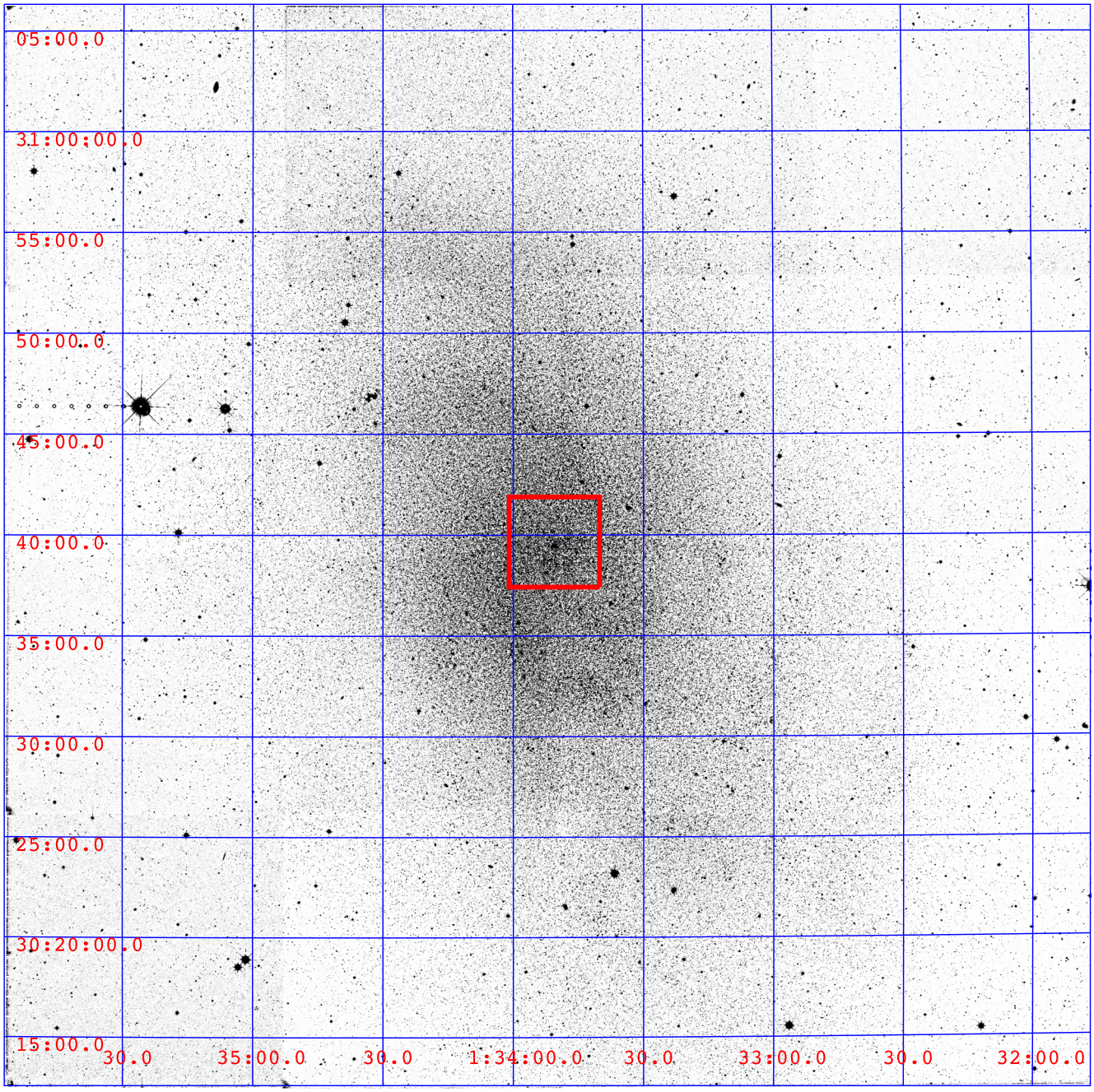

Figure 1. Combined WFCAM *K*-band mosaic of M33. The previously investigated, square-kpc area is delineated with a box.

2.2 Images

We present the combined, square degree mosaic of M33 in the *K* band in Fig. 1. The previously investigated, square-kpc area is delineated with a box. While the spiral structure is evident, the images are much less affected by extinction by interstellar dust than images at optical wavelengths. The very bright Galactic foreground red giant HD 9687 ($1^{h}35^{m}26^{s}$, $+30^{\circ}46'.5$) has left a trail of ghost imprints to its east, but saturation is not normally a problem across the mosaic. Most stars above the tip of the red giant branch (RGB) are resolved also with WFCAM, except within the central few arcsec dominated by the nuclear star cluster.

2.3 Cross-correlation of catalogues

The photometric catalogues of M33 were retrieved from the public WFCAM Science Archive (WSA). Only the overlapping area of the other catalogues (and images) with those from our own programme will be considered here; they are meant to provide further epochs that increase the sensitivity and reliability of the variability detection.

The FITS catalogues contain only un-calibrated fluxes (f, in counts) obtained in a series of apertures. By knowing the photometric zero-point at unity airmass, m_0, the extinction coefficient, a (Krisciunas et al. 1987), the airmass at the start and end of observation, $z_{\rm start}$

and $z_{\rm end}$, and exposure time, t, the (telluric) extinction-corrected and flux-calibrated magnitudes, m, are determined by

$$m = m_0 - 2.5 \log\left(\frac{f}{t}\right) - a \times \left(\frac{z_{\rm start} + z_{\rm end}}{2} - 1\right). \quad (1)$$

In order to determine the mean magnitude and light curve of all stars over the epochs in which they were detected, unique IDs need to be assigned to all individual stars. To this aim, we cross-identified each star within every catalogue. The matches were obtained by performing search iterations using growing search radii, in steps of 01 arcsec out to 1 arcsec, on a first-encountered first-associated basis but after ordering the principal photometry in order of diminishing brightness (to avoid rare bright stars being erroneously associated with any of the much larger number of faint stars).

2.4 Photometric calibration

Given the high level of crowding especially towards the central parts of M33, and the importance of accurate relative photometry between epochs in order to correctly separate variable from non-variable sources, it is essential to check the accuracy of the WSA catalogues. To this aim, we performed PSF photometry using the DAOPHOT package within IRAF (Stetson 1987) on one of the frames (from camera 1) in the central part field M33-3. An empirical constant PSF model with a 2D elliptical Gaussian function was used to construct the PSF from seven isolated stars. Then, the ALLSTAR task was used to estimate the instrumental magnitude for 32 627 stars identified with the DAOFIND task. The transformation factor from instrumental magnitude to standard magnitude was obtained from the standard magnitudes of 30 stars in common from the UIST catalogue (Paper I), hence deriving m_0 for the WFCAM data.

The celestial coordinates of the stars were calculated using the IRAF CCMAP–CCTRAN tasks. In this frame, the WSA catalogue lists 36 301 stars. We cross-identified these with the DAOPHOT catalogue within a search radius of 1 arcsec; hence, 24 140 stars were identified in common. Fig. 2 shows the difference in magnitude between the WSA and DAOPHOT photometry, against the WSA magnitude; the histogram of magnitude differences is shown in Fig. 3. The vast majority of stars have magnitudes that are consistent between the two methods of measurement within a few tenths of a magnitude; among the 3.5 per cent of stars with $\Delta m > 1$ mag, 78 per cent are located near (within 5 arcmin of) the centre of M33 where crowding is more severe than elsewhere in the mosaic. This renders just 0.9 per cent of stars with suspect photometry. Upon visual inspection of the image, it was found that in most cases there is a faint star near a bright star, and the photometric difference is simply the result of erroneous cross-identification. Consequently, the accuracy of the WSA magnitudes is acceptable.

2.4.1 *Relative calibration*

The relative calibration between frames was obtained from the mean magnitudes of ≈1000 stars in common within the magnitude interval $K \in [16, \ldots, 18]$. While these will include some variable stars, the vast majority will not vary by more than 10 per cent rendering their mean magnitude accurate to well within a per cent. Then the photometry from the different frames was brought in line with each other by applying corrections that equalised these mean magnitudes. The corrections are shown in Fig. 4, also for the UIST survey (they were not shown in Paper I). Note that the corrections are small – generally a few per cent and always less than 10 per cent.

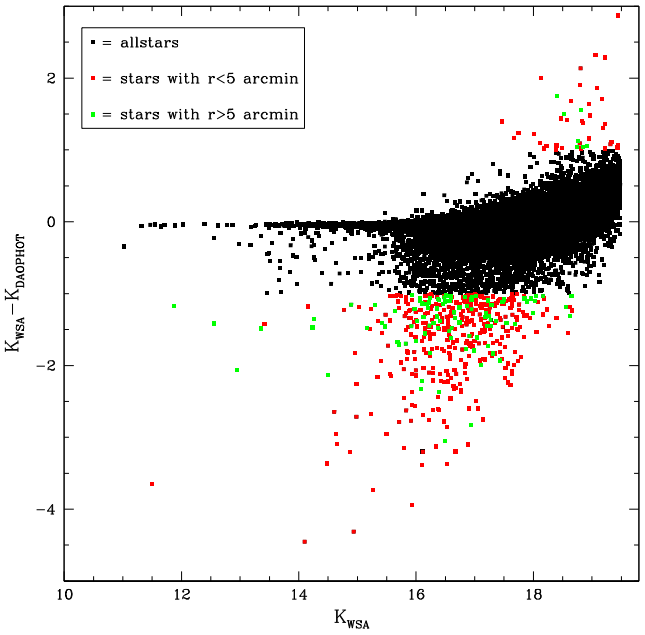

Figure 2. Magnitude differences between WSA (aperture) and DAOPHOT (PSF) photometry, plotted against WSA magnitude. Stars for which $\Delta m > 1$ mag have been identified based on whether they are located within the central 5 arcmin or further away from the unresolved centre of M33.

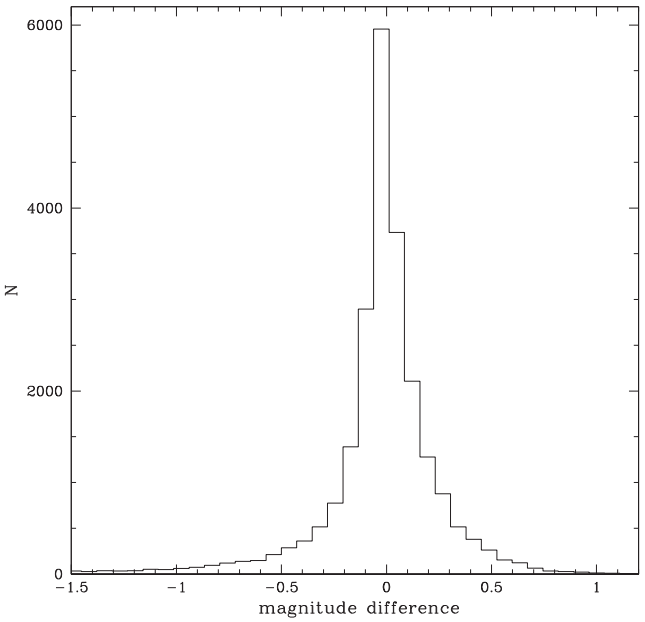

Figure 3. Histogram of the magnitude differences between WSA (aperture) and DAOPHOT (PSF) photometry.

3 VARIABILITY ANALYSIS

The search for variable stars was done by calculating the variability index for each star. This index was introduced by Welsh & Stetson (1993) and developed further by Stetson (1996). In this method, first the observations are paired on the basis of timespan between observations such that the observations of each pair have a timespan less than the shortest period expected for the kind of variable star of interest. In case more than two observations were performed within

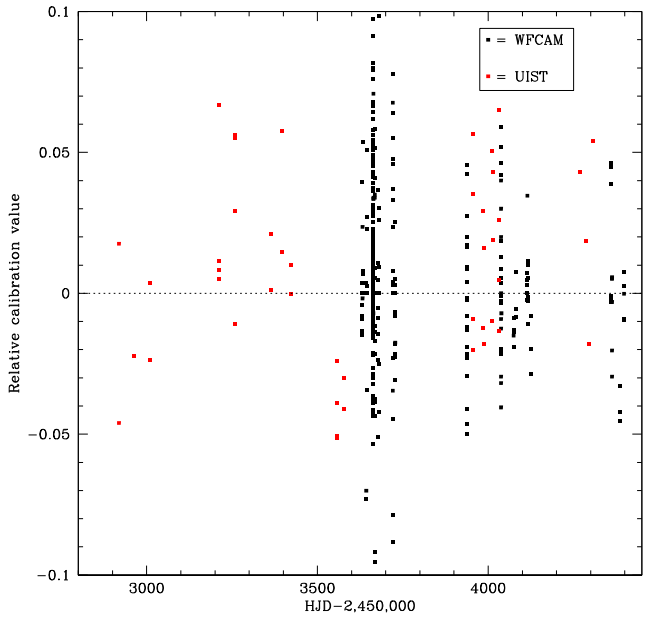

Figure 4. Relative calibration values added to the magnitudes in each of the individual frames, as a function of time, over the duration of the UIST and WFCAM monitoring campaigns.

the timespan of shortest periodicity, those sets of observations would be paired in more than one pair. Hence, the J index is calculated:

$$J = \frac{\Sigma_{k=1}^{N} w_k \ \mathrm{sign}(P_k)\sqrt{|P_k|}}{\Sigma_{k=1}^{N} w_k}. \quad (2)$$

Here, observations i and j have been paired and for each pair a weight w_k is assigned; the product of normalized residuals, $P_k = (\delta_i \delta_j)_k$,[1] where $\delta_i = (m_i - \langle m \rangle)/\epsilon_i)$, is the residual of measurement i from the mean magnitude, normalized by the error of the measurement, ϵ_i; and N is the total number of observations. Note that δ_i and δ_j may refer to observations taken in different filters. The J index for non-variable stars is approximately zero as the residuals arising from random noise are uncorrelated and their product will therefore tend to zero for large sets of measurements.

The effect of a small number of observations or corrupt data can be limited by means of a backup index, viz. the Kurtosis index:

$$K = \frac{\frac{1}{N}\Sigma_{i=1}^{n}|\delta_i|}{\sqrt{\frac{1}{N}\Sigma_{i=1}^{N}\delta_i^2}}. \quad (3)$$

The shape of the light variations define the value of the Kurtosis index; for example, $K = 0.798$ for a Gaussian distribution which is concentrated towards the average brightness level (as would be random noise), and $K \to 0$ for data affected by a single outlier (when $N \to \infty$).

Here, we use the variability index L (Stetson 1996):

$$L = \frac{J \times K}{0.798}\frac{\Sigma w}{w_{\mathrm{all}}}, \quad (4)$$

where Σw is the total weight assigned to a given star and w_{all} is the total weight a star would have if observed in every single observation.

Fig. 5 shows how the variability index L varies with K-band magnitude. For comparison with our previous UIST survey

[1] Following Stetson (1996), $P_k = \delta^2 - 1$ if $i = j$.

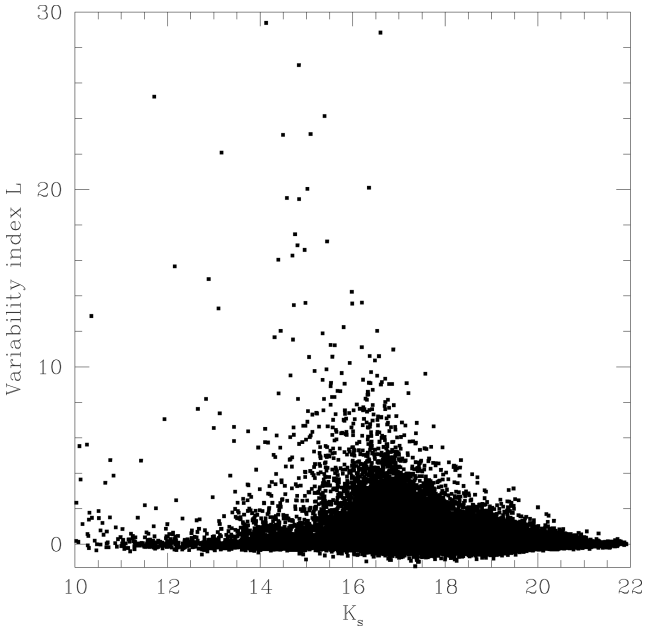

Figure 5. Variability index L *versus* K-band magnitude.

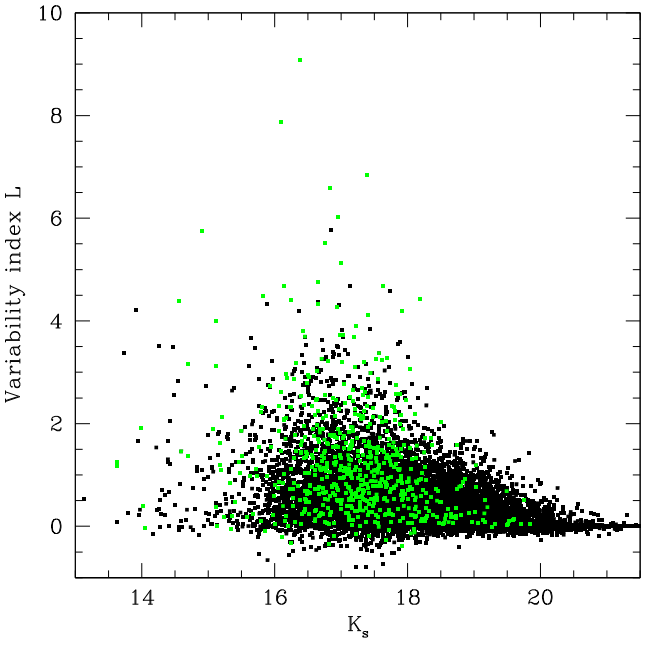

Figure 6. Variability index L versus K-band magnitude (from the WFCAM data) for the central square-kpc field that was monitored with UIST (Paper I). The green points are the UIST variable stars that were detected with WFCAM.

(Paper I), in Fig. 6 we show the distribution for the central square kpc of M33, where we indicate the WFCAM detections of stars that had been identified as variable in the UIST survey. Both graphs reveal a noticeable 'branch' of stars with larger than usual L between $K \sim 16$–18 mag; these are likely AGB stars with Mira-type variability.

Several tests were performed to select the optimal variability index threshold. First, we inspected the histograms of variability index within several magnitude bins in the range 16–19 mag for all detected stars including the M33 disc and central regions (Fig. 7).

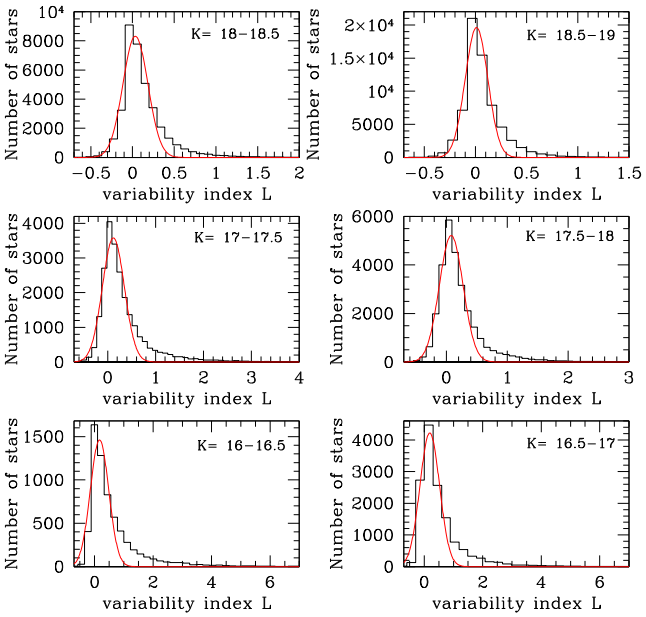

Figure 7. Variability index L histograms for several magnitudes bins in the range $K_s = 16$–19 mag. Red lines trace the Gaussian function fitted to each histogram.

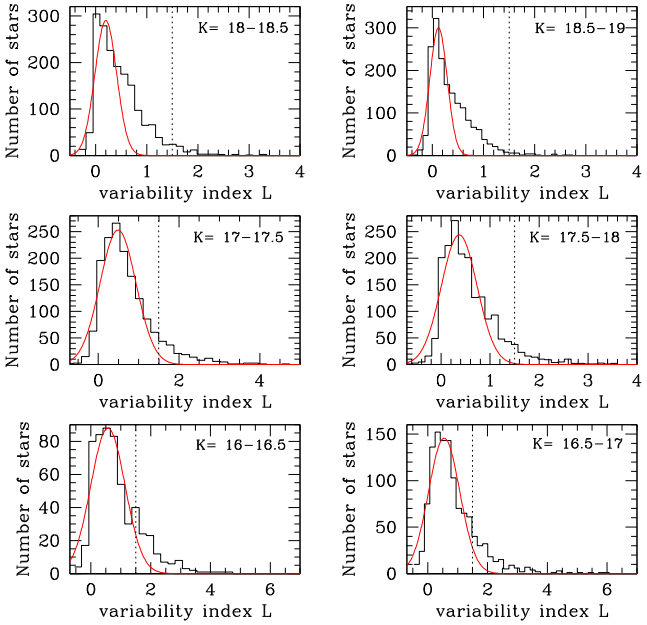

Figure 8. As Fig. 7, but limited to the central square kpc of M33. The vertical dotted line marks the limit which is used for selection of variable stars in this part of M33.

To determine the variability index threshold, a Gaussian function was fitted to each of these histograms. The Gaussian function should be near-perfectly fitted to those data for low values of L, while it departs from the histograms for larger values of L. This appears to happen around $L \sim 0.8$ but at smaller values for faint stars; we thus decided, in first instance, to set the threshold at $L > 0.7$ for the detection of variability.

Next, we test our procedure by comparing the WFCAM selected variables, with $L > 0.7$, with the UIST catalogue of variables in the central square kpc (from Paper I). The percentage of WFCAM variables within the magnitude ranges shown in Fig. 7 is about twice that derived from the UIST survey. If anything, the opposite would be expected as the UIST survey had a superior cadence of observations. Indeed, when selecting only stars from this central region of M33, the histograms of variability index broaden, and a more appropriate threshold would be $L > 1.5$ (Fig. 8). On the other hand, a threshold of $L > 0.7$ seems appropriate for the disc of M33, i.e. excluding the central square kpc (Fig. 9).

To further assess the validity of the choice of variability index threshold, we examined the location of the putative variable stars in a colour–magnitude diagram (CMD), for different choices of L threshold: $L > 0.7$, $L > 1$ and $L > 1.5$ (Fig. 10). While there is no clear difference in the selection of variable stars on the AGB and RSG portions of the CMD (roughly at $K_s = 14$–18.5 mag and $(J - L_s) > 0.8$ mag), all but the $L > 1.5$ thresholds result in many putative variable stars at fainter magnitudes and along the blue and bright vertical sequence (around $(J - K_s) \sim 0.5$ mag) where no large-amplitude red giant variables are expected.

Finally, we inspected the radial distribution of putative variable stars for the case where we apply different choices for the L threshold for the central square kpc and the (remainder of the) disc, as compared to applying a single threshold for all (Fig. 11). The former case results in a break in gradient around $r \sim 500$ arcsec – i.e. well outside the central square kpc – where $L > 0.7$ results in a seemingly disproportionally increased number of variable stars

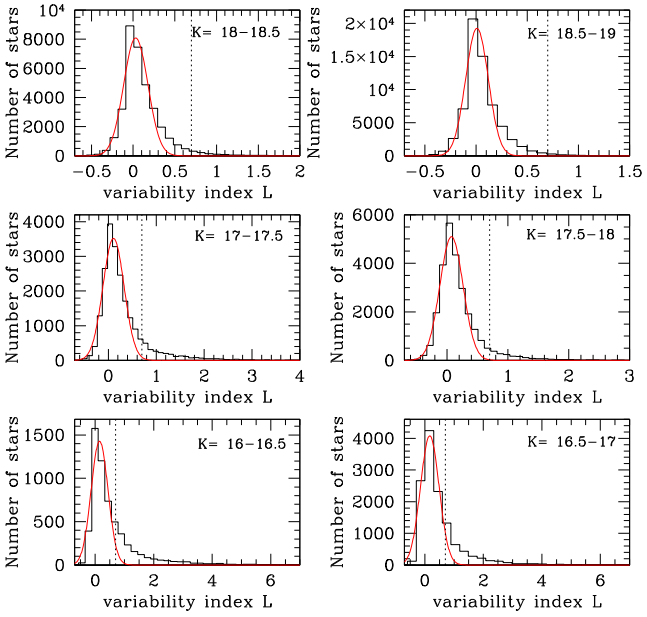

Figure 9. As Fig. 8, but now excluding the central square kpc.

closer to the centre. This gradient is not sustained within the central $r \sim 150$ arcsec – i.e. corresponding roughly to the central square kpc. Indeed, the distribution turns over and much fewer variable stars are identified once $L > 1.5$ was applied. The same artificial behaviour is not seen when the same L threshold is applied across the entire M33 galaxy.

Based on the histograms, CMD and radial distributions we decided to apply a single variability threshold of $L > 1.5$.

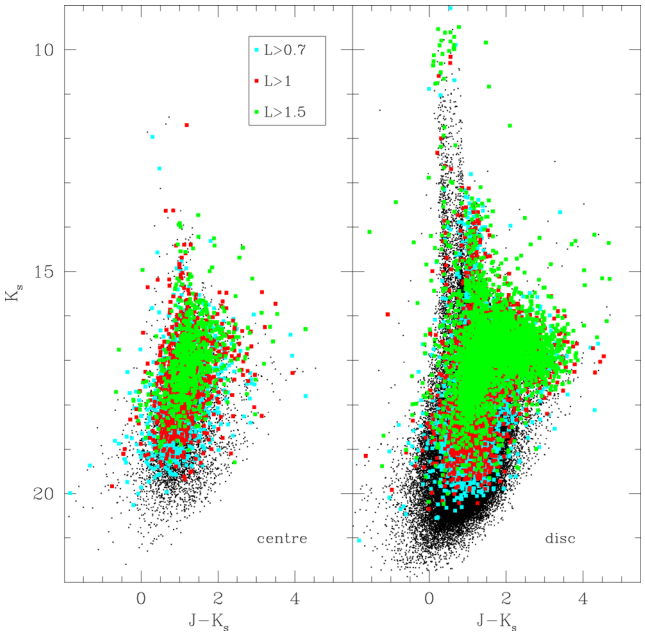

Figure 10. Near-IR colour–magnitude diagram of M33 with indicated the putative variable stars according to three choices of variability index L threshold, for (left:) the central square kpc and (right:) the disc.

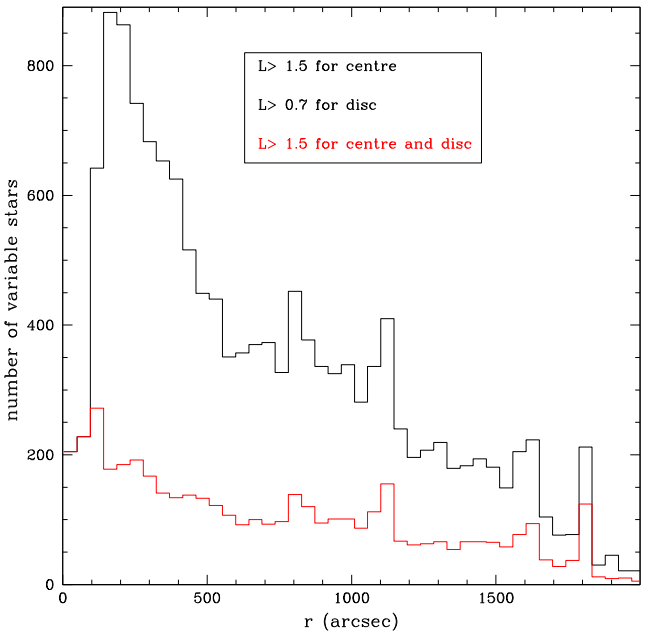

Figure 11. Radial distribution of putative variable stars where (left:) different variability index L thresholds were applied for the central square kpc and the disc and (right:) the same thresholds were applied.

3.1 Comparison between the WFCAM and UIST catalogues of variable stars within the central square kpc

One final assessment of the variability detection success is made by a more careful comparison of the common area of the WFCAM and UIST surveys. After sorting both catalogues in order of diminishing brightness in K band, matches were obtained through successive search iterations using increasing search radii, in steps of 01 arcsec out to 1 arcsec. Within the coverage of UIST (Paper I), using WFCAM, we detected 11 114 stars; from 18 398 stars detected with

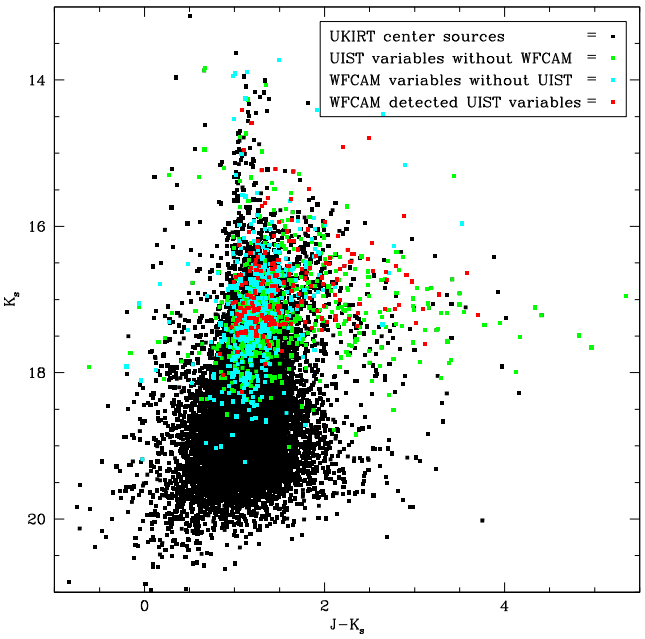

Figure 12. Near-IR CMD of the central square kpc of M33, showing those stars from the UKIRT/WFCAM survey that were and were not detected in the UKIRT/UIST survey (Paper I). A variability threshold of $L > 1.5$ was applied to select variable stars from the WFCAM survey.

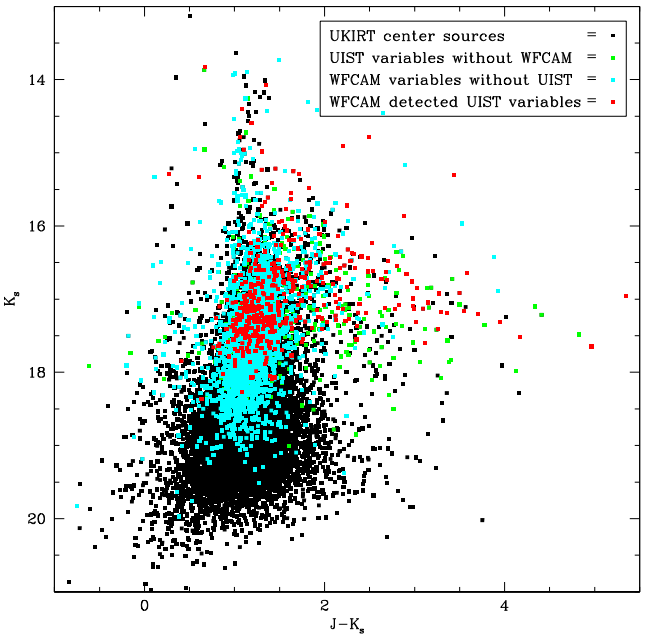

Figure 13. Same as Fig. 12, but for a threshold of $L > 0.7$.

UIST, using WFCAM we detected 10 095 stars. Applying $L > 1.5$, we find 667 variable stars located within the central square kpc covered by UIST (out of 4643 in total across the WFCAM coverage); applying $L > 0.7$, this becomes 2696 – i.e. more than three times as many as were found in the more capable UIST survey. Again applying $L > 1.5$, only 192 out of the 812 UIST LPVs were identified with WFCAM (a success rate of 24 per cent). This also suggests that the UIST survey, too, is incomplete.

Figs 12 and 13 show CMDs in which are highlighted those variable stars which have and those which have not been detected with

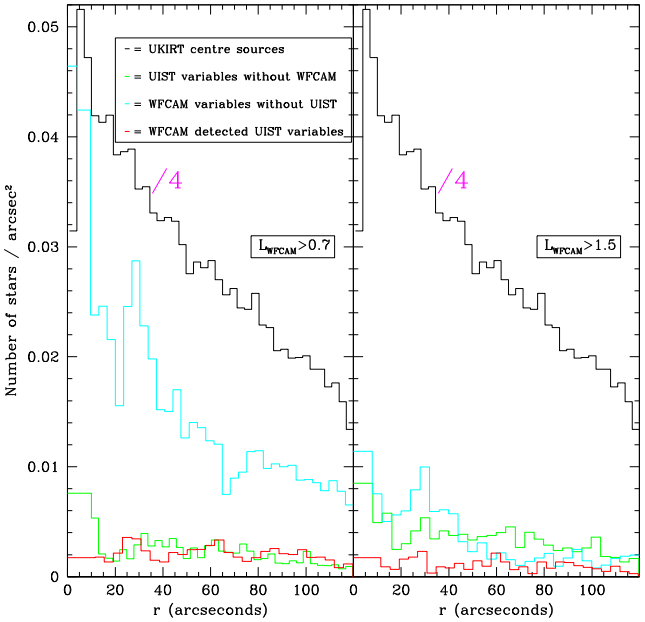

Figure 14. Radial profiles of total stellar density (divided by four for ease of comparison) and density of variable stars found in the WFCAM and/or UIST surveys, applying a variability index threshold of $L > 0.7$ (left) and $L > 1.5$ (right), respectively.

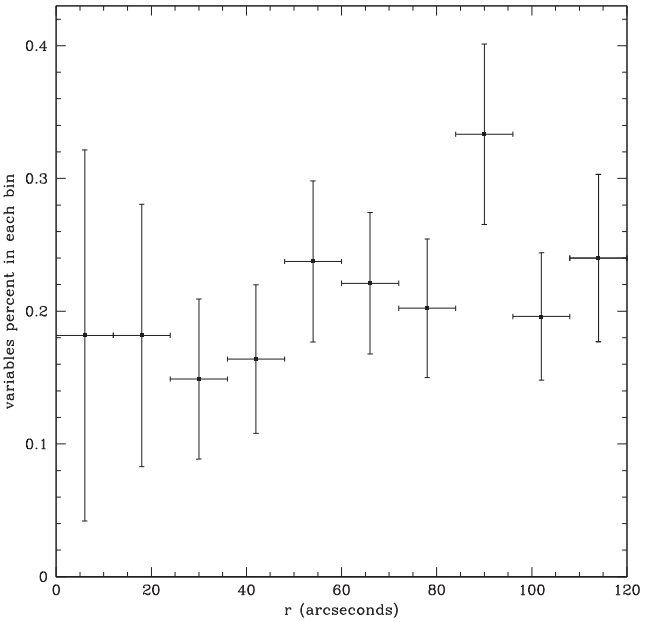

Figure 15. Radial profile of the fraction of UIST variables that is recovered in the WFCAM variability survey.

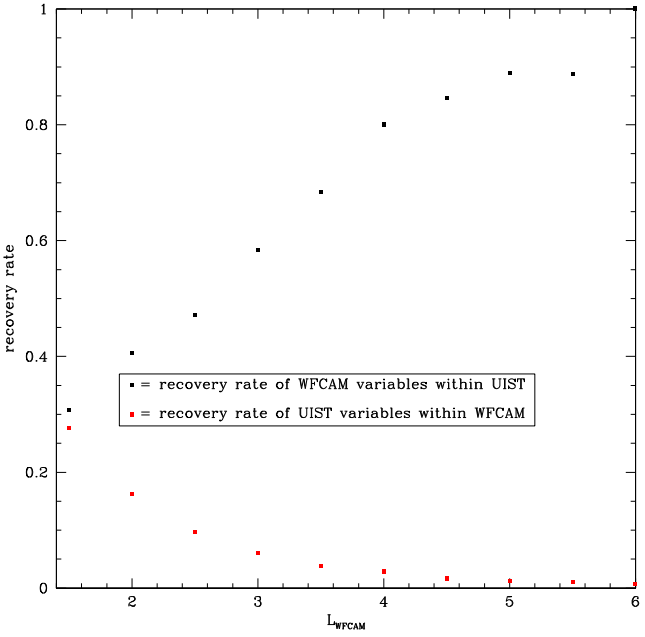

Figure 16. Recovery rate of UIST variable stars within the WFCAM survey, and vice versa, as a function of WFCAM variability index threshold (L).

either WFCAM of UIST, when applying a WFCAM variability index threshold of $L > 1.5$ and $L > 0.7$, respectively. These CMDs suggest that $L > 1.5$ is a more sensible threshold than $L > 0.7$, for two reasons; first, it yields a somewhat smaller number of variables with WFCAM than with UIST, which is expected as WFCAM has more difficulty in isolating blended stars and also the WFCAM survey is based on fewer epochs. Secondly, the fraction of UIST variables that were found with WFCAM is smaller but the fraction of WFCAM variables that were found with UIST is much larger (31 per cent) than when applying $L > 0.7$ (14 per cent).

Since the central part of M33 comprises a considerable variation in stellar density, the same data displayed in Figs 12 and 13 are shown in Fig. 14 as a function of radial distance from the centre of M33. The rate at which variable stars are detected increases towards the centre, and as a consequence the number of variable stars found in one of the surveys that is not recovered within the other survey also increases towards the centre. However, when applying a variability index threshold of $L_{\rm WFCAM} > 0.7$, the WFCAM survey yields many more variable stars than the UIST survey, whilst for $L_{\rm WFCAM} > 1.5$ this is about equal. This again favours the choice of the latter threshold. The success rate of the WFCAM survey to recover UIST variable stars displays only a shallow gradient with radial distance from the centre of M33 (Fig. 15); it averages ∼22 per cent for this central region (but is ∼24 per cent for the square area encompassing this circular area).

The recovery rate of UIST variables within the WFCAM catalogue of variable stars, and vice versa, is plotted as a function of WFCAM variability index threshold in Fig. 16. At $L_{\rm WFCAM} > 1.5$, a near-equal fraction of variable stars is recovered within each of the surveys (∼30 per cent) – the UIST survey is slightly more successful than the WFCAM survey, as expected (see above). As $L_{\rm WFCAM}$ increases, the number of variable stars identified in the WFCAM survey decreases but these variable stars will be the ones with larger amplitudes. Hence, the UIST survey will be more complete in including those WFCAM variable stars, reaching ∼90 per cent success rate for $L_{\rm WFCAM} > 5$. On the other hand, the WFCAM survey will miss more of the UIST variable stars (generally the ones with smaller amplitudes), and its success rate drops to just one per cent for $L_{\rm WFCAM} > 5$. Hence, the choice for $L_{\rm WFCAM} > 1.5$ is supported once again.

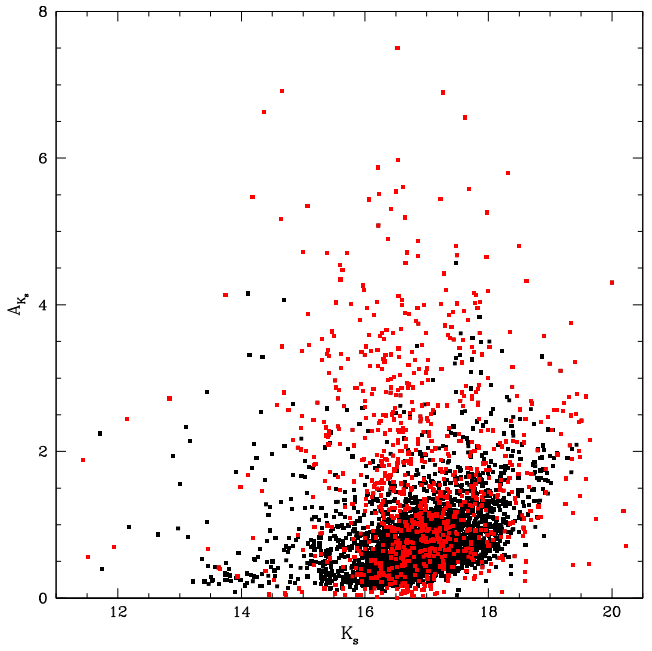

Figure 17. Estimated amplitude, A_K, of variability versus K-band magnitude. Stars with ≤6 measurements are highlighted in red.

3.2 Amplitudes of variability

We estimate the amplitude of variability by assuming a sinusoidal light curve shape. The amplitude is then

$$A \approx 2 \times \sigma / 0.701, \quad (5)$$

where σ is the standard deviation in our data and 0.701 is the standard deviation of a unit sine function. The standard deviation is uncertain when the number of measurements (N) is small; we showed in Paper I that $N = 6$ is the minimum acceptable to reach ∼10 per cent fidelity.

The estimated K-band amplitude is plotted *versus* K-band magnitude in Fig. 17. As is well known by now (Wood et al. 1992; Wood 1998; Whitelock et al. 2003; Paper I), the amplitude of variability exhibits a clear tendency to diminish with increasing brightness, which is partly due to the definition of magnitude as a relative measure rather than less powerful pulsation (van Loon et al. 2008). The amplitude is generally about a magnitude or less, but a small fraction of variable stars (8 per cent) seem to reach $A_K > 2$ mag. Very dusty AGB stars – which are rare – are known to reach such large amplitudes (Wood et al. 1992; Wood 1998; Whitelock et al. 2003). Among these extreme variables, 311 stars have $N \leq 6$; excluding these stars, only 20 stars remain with $A_K > 3$ mag. The brightest variables, with $K_s < 13$ mag, are foreground red giants; among the faintest stars, with $K_s > 17$ mag, our survey becomes increasingly less sensitive to small-amplitude variables.

4 DESCRIPTION OF THE CATALOGUE

The photometric catalogue including all variable and non-variable stars is made publicly available at the CDS. The content is described in Table 4. It is composed of two parts, part I comprising the mean properties of the stars and part II tabulating all the photometry (for the benefit of generating light curves, for instance).

The astrometric accuracy of the catalogue is ≈0.2 arcsec rms, tied to the 2MASS system. This accuracy was found to be consistent with the results from our cross-correlations with three other optical and IR catalogues (cf. Section 5.3).

Table 4. Description of the photometric catalogue.

Column no.	Descriptor
Part I: stellar mean properties (403 734 lines)	
1	Star number
2	Right ascension (J2000)
3	Declination (J2000)
4	Mean J-band magnitude
5	Error in $\langle J \rangle$
6	Mean H-band magnitude
7	Error in $\langle H \rangle$
8	Mean K-band magnitude
9	Error in $\langle K \rangle$
10	Number of J-band measurements
11	Number of H-band measurements
12	Number of K-band measurements
13	Variability index J
14	Kurtosis index K
15	Variability index L
16	Estimated K-band amplitude
Part II: multi-epoch data (3623 332 lines)	
1	Star number
2	Epoch (HJD–2450000)
3	Filter (J, H, or K)
4	Magnitude
5	Error in magnitude

5 DISCUSSION

5.1 The near-IR variable star population

Fig. 18 presents near-IR CMDs for the whole region of M33 monitored with WFCAM. The large-amplitude variable stars we identified are highlighted in green. These are mainly found between $K_s \sim 16$ and 18 mag, and are largely absent among fainter stars

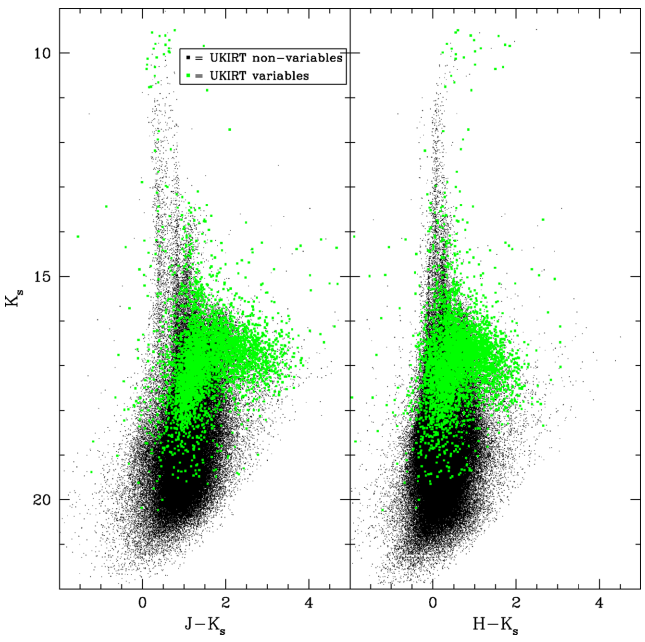

Figure 18. Near-IR CMDs (WFCAM variable stars in green).

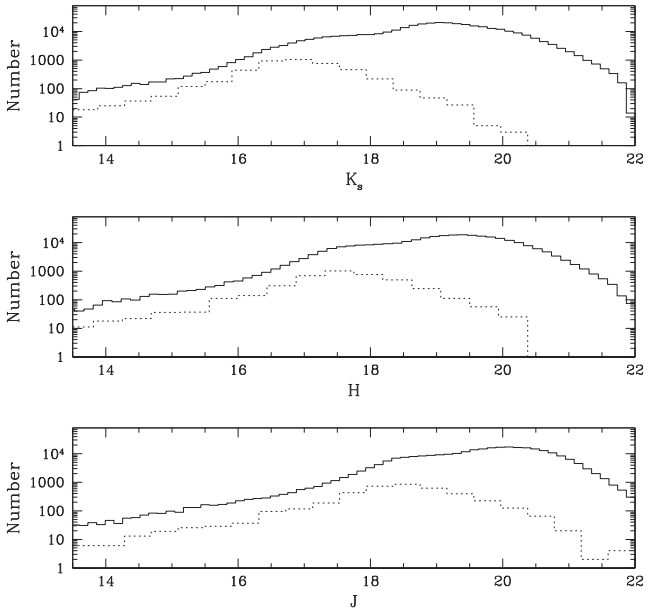

Figure 19. Distribution of all WFCAM sources (solid) and the variable stars (dotted), as a function of near-IR brightness.

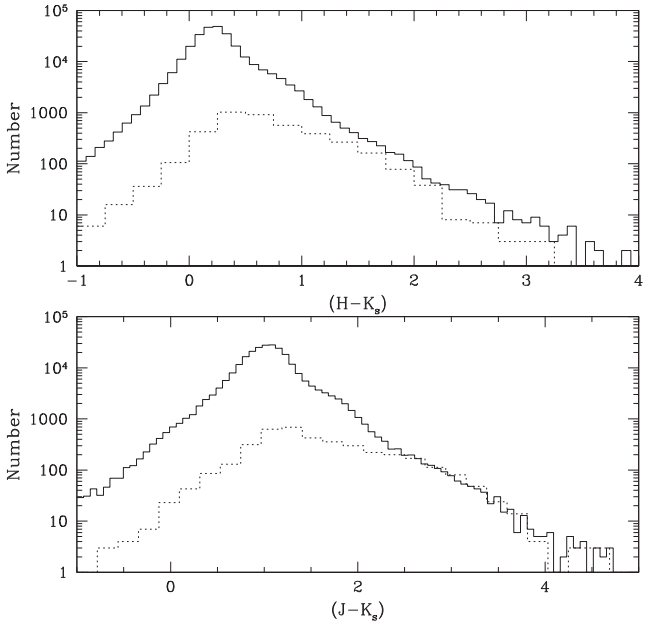

Figure 20. Distribution of all WFCAM sources with $K_s < 19$ mag (solid) and the variable stars (dotted), as a function of near-IR colour.

(below the tip of the RGB at $K_s \sim 18$ mag). Some brighter variable RSGs are found (around $K_s \sim 14$ mag), but the clump of variables stars with $K_s < 11$ mag and redder colour in $H - K_s$ than $J - K_s$ are foreground stars and perhaps saturated. Variable stars dominate the redder stars to the right of the vertical sequence comprising the bulk of stars.

The distributions over brightness (Fig. 19) and colour (Fig. 20) provide another means of assessing the properties of the variable stars. The largest fraction of stars that are found to be variable occurs between $K_s \sim 16$ and 17 mag, albeit less than that of the UIST survey in the central region in the same magnitude interval. The variable star population reaches a peak around $K_s \sim 17$ mag; it then

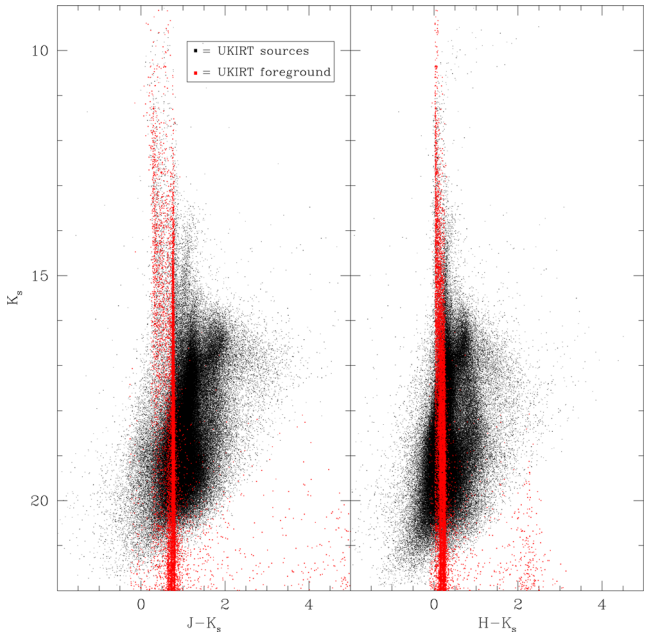

Figure 21. Estimated contamination by foreground stars (in red), from a simulation with TRILEGAL (Girardi et al. 2005).

drops at fainter magnitudes even though the total stellar population keeps increasing. This mainly arises from two factors: first, many stars in this magnitude interval have not yet reached the final phase of their evolution and they will still evolve to higher luminosities and lower temperatures before they develop large-amplitude variability; secondly, the birth mass and *K*-band brightness relation flattens considerably for low-mas AGB stars (see Paper II). At $(J - K_s) > 2$ mag or $(H - K_s) > 1$ mag, almost all stars ($K_s < 19$ mag) are variable; these are dusty, strongly pulsating and heavily mass-losing AGB stars.

The level of contamination by foreground stars can be assessed with the TRILEGAL simulation tool (Girardi et al. 2005). We used default parameters for the structure of the Galaxy, simulating a 0.9 deg^2 field in the direction ($l = 133.^\circ61$, $b = -31.^\circ33$). Only a relatively small number of foreground stars are expected, with fairly neutral colours or below our completeness limit (Fig. 21). The part of the CMD occupied by large-amplitude variable stars is relatively uncontaminated by foreground stars.

The stellar populations can be described using isochrones calculated by Marigo et al. (2008, Fig. 22). The isochrones were calculated for solar metallicity ($Z_\odot = 0.015$) for all stellar populations except the oldest, least chemically evolved one with $\log t[\mathrm{yr}] = 10$ for which we adopted $Z = 0.008$. To account for a (shallow) metallicity gradient across the disc of M33, we show CMDs of each of the 16 tiles of the M33 mosaic, overlain with isochrones for $Z = 0.015$ in the central region but $Z = 0.008$ further out in the disc (Fig. 23).

The isochrones from Marigo et al. (2008) are the most realistic models to be used for the purpose of this study, for the following reasons.

(i) The star's evolution is followed all the way through the thermal pulsing AGB until the post-AGB phase. Crucially, two important phases of stellar evolution are included, viz. the third dredge-up mixing of the stellar mantle as a result of the helium-burning phase, and the enhanced luminosity of massive AGB stars undergoing hot bottom burning (Iben & Renzini 1983).

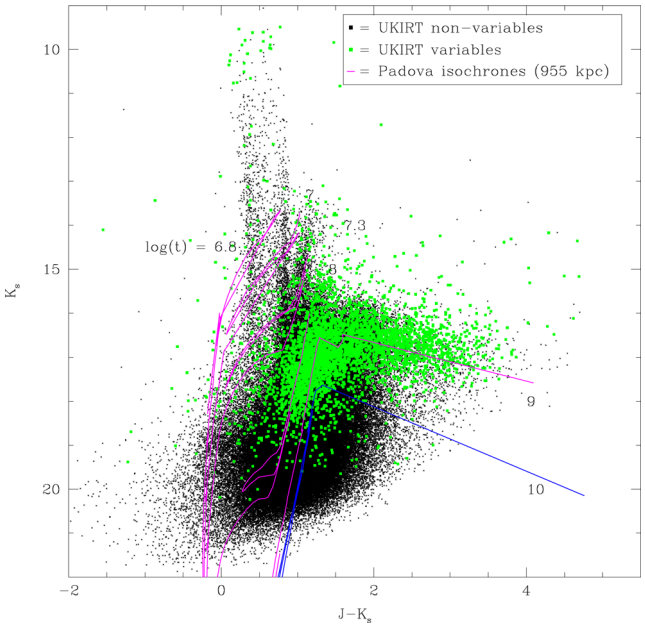

Figure 22. CMD of $(J - K_s)$, with WFCAM variable stars in green. Overplotted are isochrones from Marigo et al. (2008) for solar metallicity and a distance modulus of $\mu = 24.9$ mag.

(ii) The molecular opacities which are important for the cool atmospheres of evolved stars have been considered in the models of stellar structure. The transformation from oxygen-dominated (M-type) AGB stars to carbon stars in the birth mass range $M \sim 1.5$–$4\ M_\odot$ is accounted for (cf. Girardi & Marigo 2007).

(iii) The dust production in the winds of LPVs, and the associated reddening is included.

(iv) The radial pulsation mode is predicted.

(v) Combination of their own models for intermediate-mass stars ($M < 7\ M_\odot$), with Padova models for more massive stars ($M > 7\ M_\odot$; Bertelli et al. 1994), gives a complete coverage in birth mass ($0.8 < M < 30\ M_\odot$).

(vi) Magnitudes are calculated on a wide range of common optical and IR photometric systems.

(vii) The isochrones are available via an internet-based form, in a user-friendly format.

5.2 Spatial distribution of LPVs

Maps of the surface density of the number of large-amplitude variable stars, AGB stars, RGB stars, and massive stars are presented in Fig. 24. The same selection criteria as in Paper II are used to select these different populations: the demarcation between massive stars and less-massive giant stars is defined to run from $(J - K_s, K_s) = (0.6, 18)$ mag to $(J - K_s, K_s) = (0.9, 15.6)$ mag, such that massive stars have colours bluer than this (down to $K_s = 19.5$ mag) or have $K_s < 15.6$ mag, whilst AGB stars and RGB stars are redder than this and have $16 < K_s < 18$ mag or $18.3 < K_s < 19.5$ mag, respectively.

The variable stars, AGB stars, and massive stars are concentrated towards the centre but the RGB stars do not show such strong central concentration. This is in good agreement with what we found for the central square kpc of M33 in Paper II. The distribution of the variable stars mostly mimics that of the AGB stars, as expected, though the somewhat stronger central concentration in the former suggests that more massive stars (AGB stars as well as RSGs) make a larger contribution in the central part of M33 than further out in the disc. Only hints can be seen of the spiral arm pattern in these maps.

5.3 Cross-identifications in other catalogues

We have cross-correlated our UKIRT/WFCAM variability search results with those from two intensive optical monitoring campaigns (CFHT, Hartman et al. 2006, in Section 5.3.1; DIRECT, Macri et al. 2001, in Section 5.3.2). We have also compared with the optical catalogue of Rowe et al. (2005) which includes narrow-band filters that they used to identify carbon stars (in Section 5.3.3); RSGs from Drout et al. (2012) in Section 5.3.4; and a small number of luminous blue variable (LBV) stars from Humphreys et al. (2014) in Section 5.3.5. In addition, we compared our data with the mid-IR variability search performed with the *Spitzer* Space Telescope (McQuinn et al. 2007) in Section 5.3.6. The matches were obtained by search iterations using growing search radii, in steps of 01 arcsec out to 1 arcsec, on a first-encountered first-associated basis after ordering the principal photometry in order of diminishing brightness (K_s-band for the UKIRT catalogue, i band/I band for the optical catalogues, and 3.6-μm band for the *Spitzer* catalogue). Finally, we examined our data on the recently identified 24-μm variables (Montiel et al. 2014) which includes the giant H II region NGC 604 (in Section 5.3.7).

5.3.1 CFHT optical variability survey

A variability survey of M33 was carried out with the 3.6-m Canada–France–Hawaii Telescope (CFHT) on 27 nights comprising 36 individual measurements, between 2003 August and 2005 January (Hartman et al. 2006). Out of two million point sources in a square degree field, they identified more than 1300 candidate variable blue and RSGs, more than 2000 Cepheids, and more than 19 000 AGB and RGB LPVs. Their catalogue comprises Sloan g'-, r'- and i'-band photometry to a depth of $i' \approx 24$ mag.

Out of 36 000 variable stars detected with CFHT in our field of M33, our UKIRT/WFCAM survey detected 29 600 stars (82 per cent), of which 1818 were found by us to be variable (Fig. 25). Most of the CFHT variables that were missed in our survey are fainter than the RGB tip; these are not the type of variables that our survey aims to detect. The AGB and RSG variables that were not detected in our survey have modest amplitudes (especially at IR wavelengths). On the other hand, our survey detected some of the dustiest AGB variables that were missed by the CFHT survey.

5.3.2 DIRECT optical variability survey

The DIRECT variability survey (Macri et al. 2001) aimed to determine a distance estimate of M33 (and M 31) using detached eclipsing binaries and Cepheids. It was carried out on 95 nights with the F.L. Whipple observatory's 1.2-m telescope and on 36 nights with the Michigan–Dartmouth–MIT 1.3-m telescope, between 1996 September and 1997 October. Their catalogue contains Johnson B- and V-, and Cousins I-band photometry for all stars with $14.4 < V < 23.6$ mag, and the V-band J variability index (cf. Section 3).

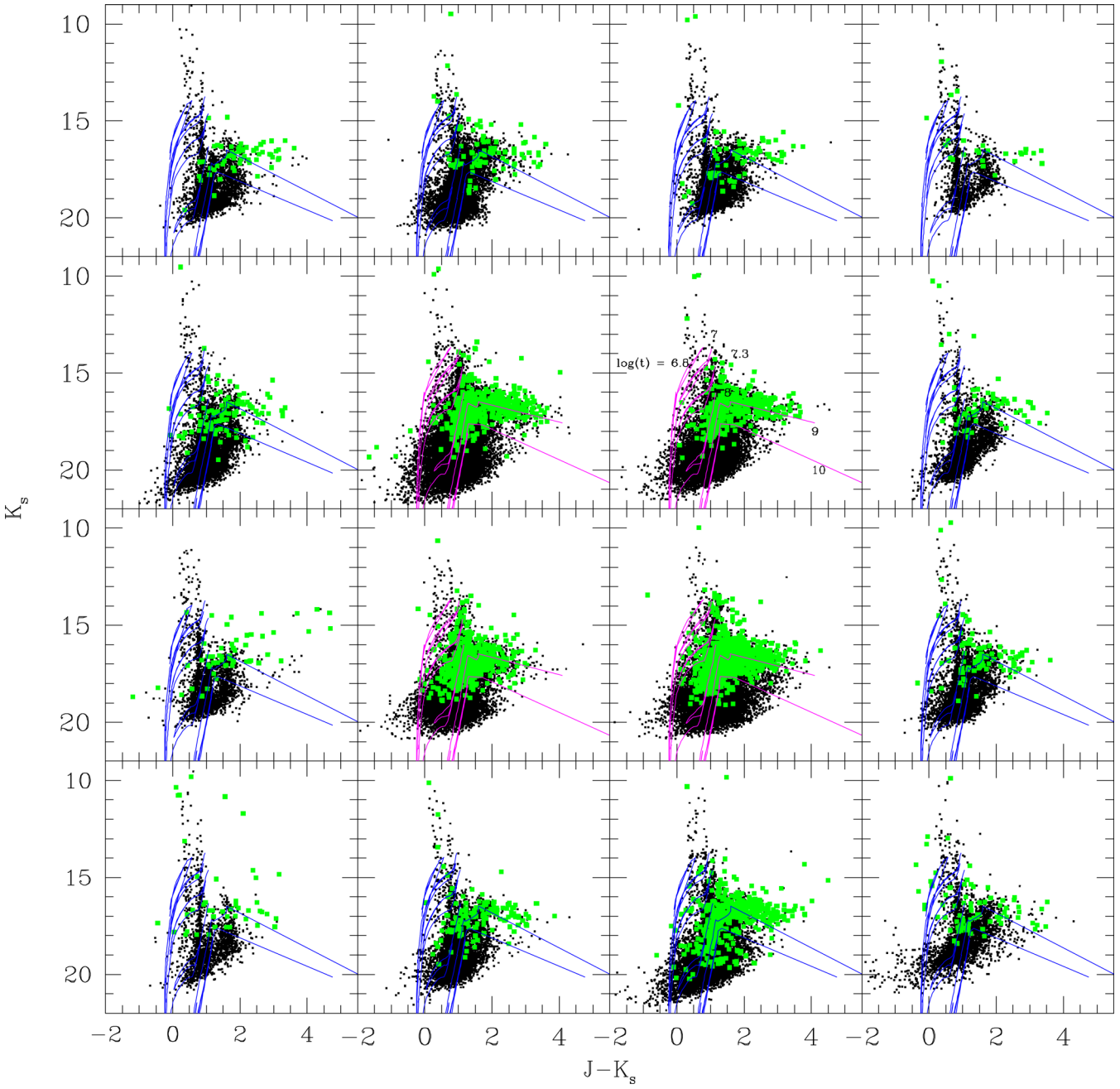

Figure 23. Near-IR CMDs of each of the individual tiles in our mosaic. The WFCAM variable stars are highlighted in green. Isochrones from Marigo et al. (2008) are overlain for $Z = 0.015$ (pink) and $Z = 0.008$ (blue).

The central region of M33 observed in DIRECT is completely covered in our WFCAM survey. The DIRECT survey listed 57 581 stars among which 1383 have $J > 0.75$ (which the DIRECT team assumed as the variability threshold). Within the coverage of DIRECT are located 116 606 stars from the WFCAM catalogue, including 1444 WFCAM variables. Of the 24 422 stars from DIRECT that were detected in our WFCAM survey, 412 were found by us to be variable. Hence, most of the WFCAM variables were missed by the DIRECT survey (Fig. 26). This is unsurprising since dusty AGB variables are faint at optical wavelengths, but the relatively short duration of the DIRECT survey (little more than a year) may have contributed to it missing also less dusty AGB variables.

5.3.3 Carbon star survey

Rowe et al. (2005) used the CFHT and a four-filter system in 1999 and 2000 to cover much of M33. The filter system was designed to identify carbon stars on the basis of their cyanide (CN) absorption as opposed to other red giants that display titanium-oxide (TiO) absorption, using narrow-band filters centred on 8120 and 7777 Å, respectively. They added broad-band Mould *V*- and *I*-band filters to aid in selecting cool stars. Carbon stars in their scheme have [CN]−[TiO] >0.3 and $V - I > 1.8$ mag, and M-type stars have [CN]−[TiO] <−0.2 mag at the same $V - I$ criterion (they only considered stars for this purpose that had errors on these colours of <0.05 mag).

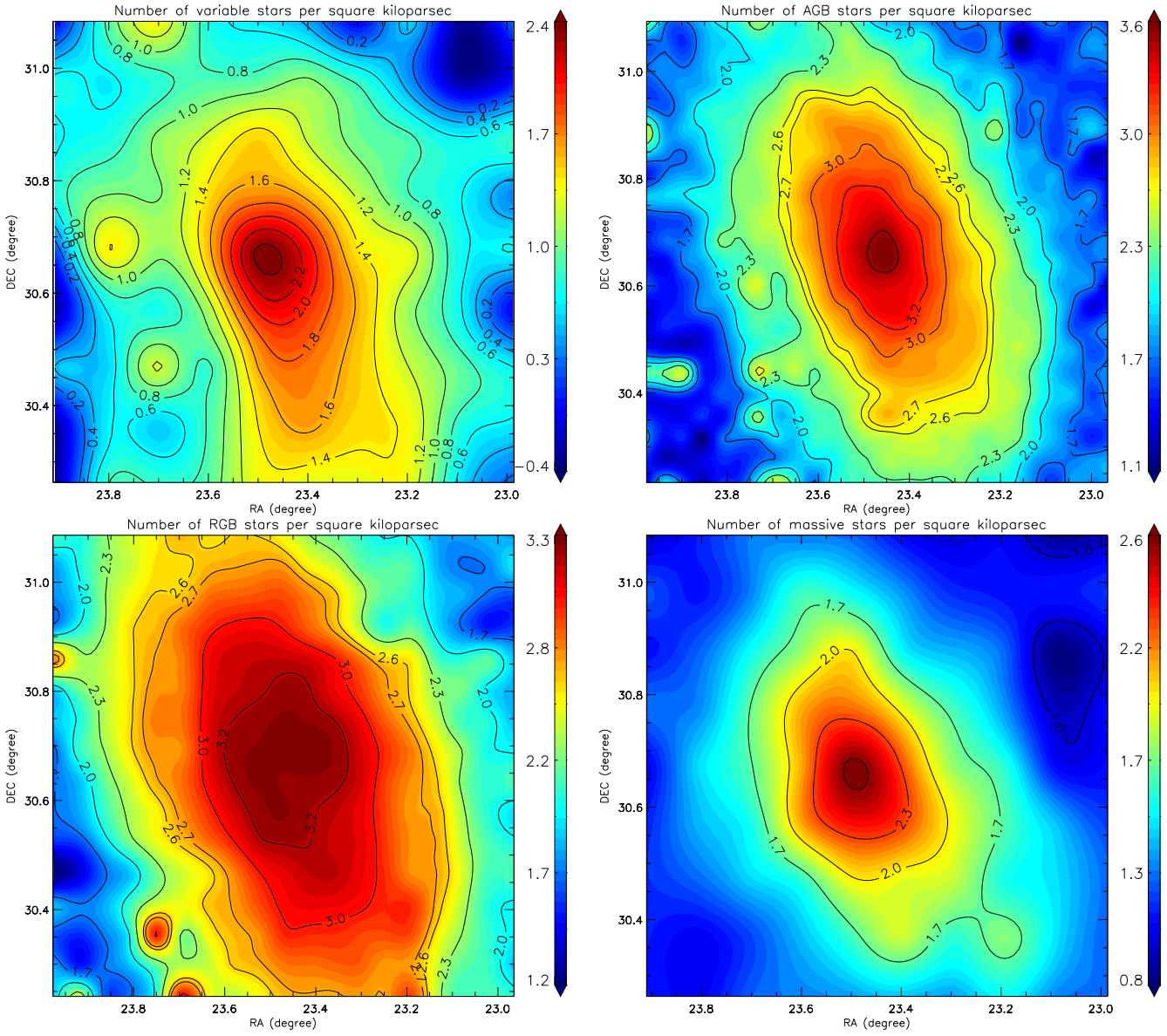

Figure 24. Spatial distribution across M33 of the near-IR populations of (top left:) WFCAM LPVs; (top right:) AGB stars; (bottom Left:) RGB stars; (bottom right:) massive stars. The units are logarithmic in number of stars per square kpc.

Within the area in common with our WFCAM survey, Rowe et al. detected 2079 334 stars, from which 306 292 stars (3.5 per cent) were identified with WFCAM (a further 85 098 stars from the WFCAM catalogue are outside of their coverage). Among these, 11 040 stars are M-type and 3134 are carbon stars. To improve the cross-correlation and to avoid coincidences because of the high density of optical sources, a pre-selection was made on carbon stars and M-type stars that are likely to have been detected at near-IR wavelengths. The average offset between the two catalogues was found to be only 002 arcsec in both RA and Dec.

The main giant branches – viz. the RSGs around $(J - K_s) \approx 0.8$ mag and the AGB around $(J - K_s) \approx 1$ mag – are traced by M-type stars, with carbon stars digressing towards redder colours at $K_s \sim 16$–17 mag (Fig. 27). The carbon star distribution is consistent with a typical $t \sim 1$ Gyr ($\log t \sim 9$) isochrone or a little younger, i.e. birth masses around 2–3 $M_\odot$. Some of the bright carbon stars show signs of reddening to $(J - K_s) > 2$ mag presumably due to circumstellar dust; as these are among the brightest detected carbon stars, they must indicate the termination point in carbon star evolution. Carbon stars are found fainter than the RGB tip, down to $K_s \sim 19$ mag; these may have formed through binary mass transfer. Such faint carbon stars are known in other, especially metal-poor populations, e.g. in the Sagittarius dwarf irregular galaxy (Gullieuszik et al. 2007) or in the Galactic globular cluster ω Centauri (van Loon et al. 2007). Note that our WFCAM survey detected large-amplitude variability in carbon stars only brighter than $K_s \approx 17.5$ mag, i.e. above the RGB tip and consistent with thermal pulsing AGB stars that have become carbon stars as a result of third dredge-up.

Fig. 28 presents a near-IR colour–colour diagram for AGB and RGB stars only, as other populations tend to confuse the picture in such diagram. Stars with $18.5 < K_s < 19.5$ mag are assumed

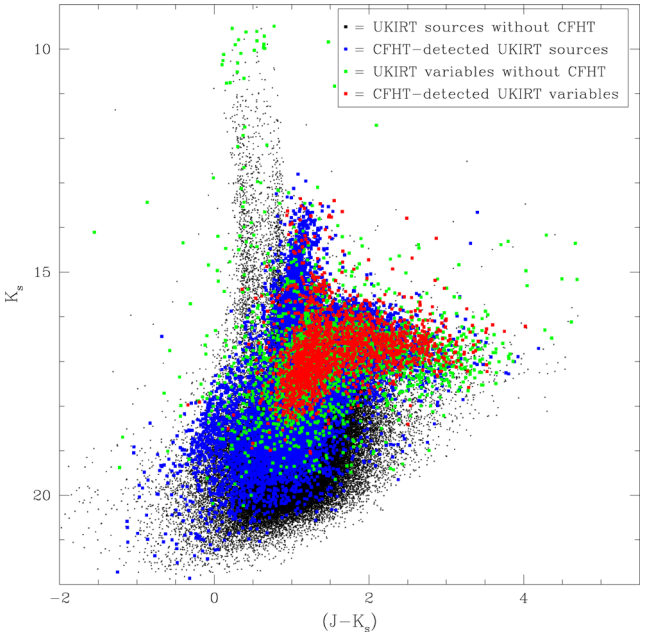

Figure 25. Near-IR CMD showing the stars from the WFCAM survey that were and were not identified as variable stars in the CFHT optical variability survey (Hartman et al. 2006).

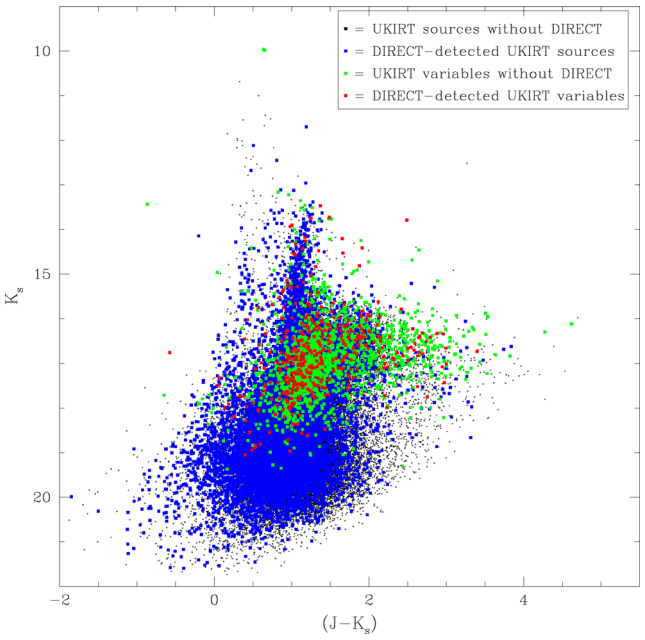

Figure 26. As Fig. 25, for the DIRECT optical variability survey (Macri et al. 2001).

to be on the RGB, whilst stars with $16 < K_s < 18$ mag are considered to be on the AGB (note that this selection excludes some of either type but maximizes the purity of these two samples). For both selections, we only kept stars with photometric errors on the colour <0.25 mag. The M-type and carbon stars classified by Rowe et al. are highlighted. Some of the M-type, but especially carbon stars follow part of a sequence towards red colours, but the reddest of these, at $(H - K_s) > 1$ mag and $(J - H) > 1$ mag have generally not been bright enough at optical wavelengths for spectral typing.

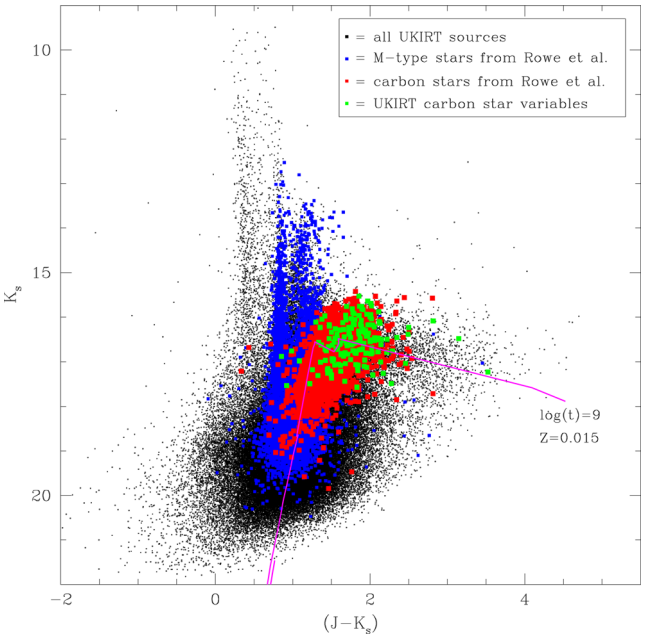

Figure 27. Near-IR CMD showing the M-type and carbon stars from the Rowe et al. (2005) survey that were detected in our UKIRT/WFCAM survey. A 1-Gyr isochrone from Marigo et al. (2008), for solar metallicity, is shown for comparison.

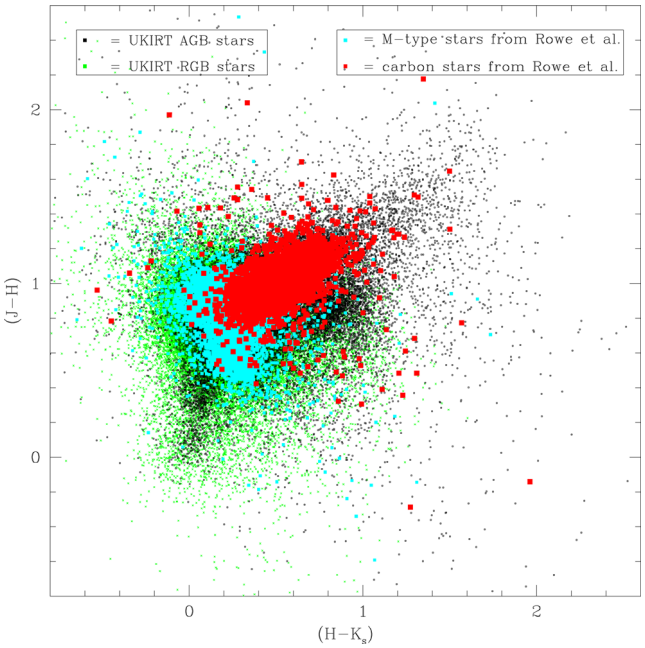

Figure 28. Near-IR colour–colour diagram showing the M-type and carbon stars from the Rowe et al. (2005) survey that were detected in our UKIRT/WFCAM survey. Stars with $18.5 < K_s < 19.5$ mag and errors on the colours <0.25 mag are labelled as RGB stars, whilst stars with $16 < K_s < 18$ mag and errors on the colours <0.25 mag are labelled as AGB stars.

These are dusty LPVs identified in our WFCAM survey. The realm of the RGB stars spreads out over colour but generally this happens in one but not both colours at once, suggesting blends and/or other photometric uncertainties are to be blamed.

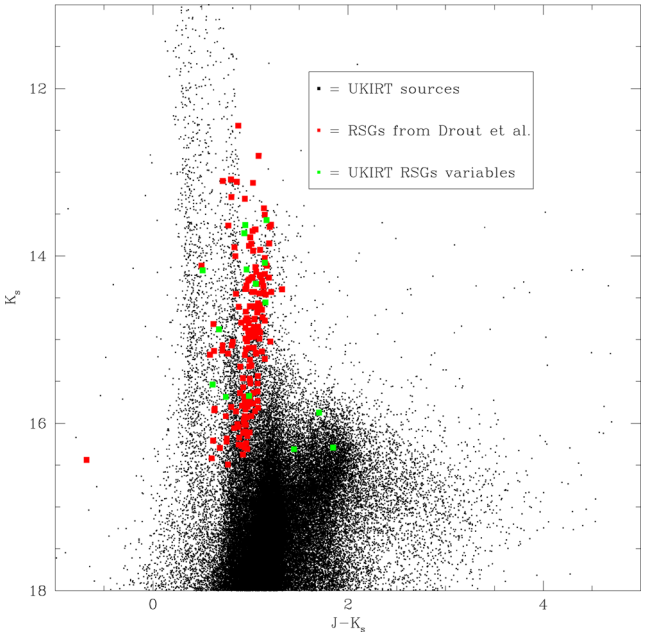

Figure 29. As Fig. 26, for the RSGs from Drout et al. (2012).

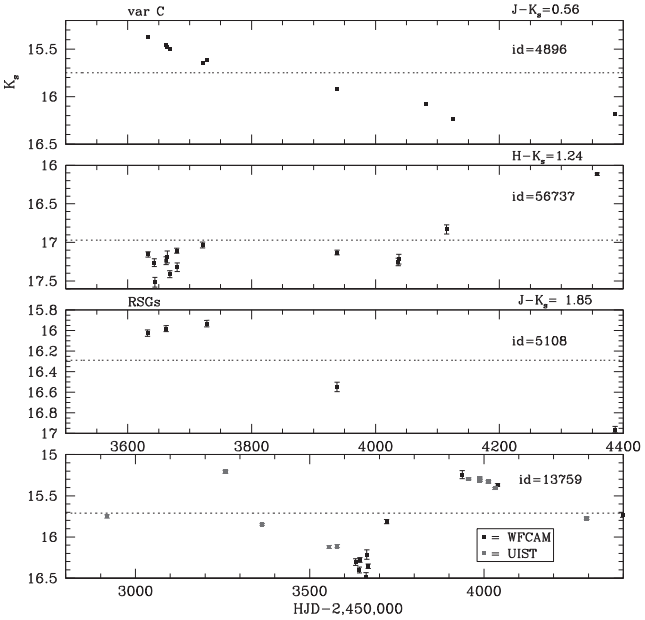

Figure 30. Light curves of selected variable stars: (top:) the LBV Var C; (middle:) two of the RSGs; (bottom:) one of the stars for which we showed the light curve in Paper I, but now based on the combined UIST+WFCAM photometry.

5.3.4 RSG stars

Drout et al. (2012) identified RSGs (and yellow supergiants) in M33 using the Hectospec multi-fibre spectrograph on the 6.5-m Multiple Mirror Telescope in two observing campaigns, in 2009 and 2010.

They divided their list in three different categories: those supergiants that were selected both photometrically and kinematically, assigned rank 1; those confirmed with just one method, assigned rank 2; and those which were not selected by either method and which are likely foreground dwarfs, assigned rank 3. They identified 189 rank-1 stars, 12 rank-2 stars, and 207 rank-3 stars.

Our WFCAM survey detected 381 of the red stars in the survey by Drout et al. (93 per cent), from which 186 rank-1 stars (98 per cent) and 13 rank-2 stars. Of the rank-1 stars, 14 were found by us to be variable, as was one rank-2 star. Their RSGs clearly delineate a branch in the near-IR CMD (Fig. 29; see also Fig. 30). It is possible that some of the reddened sources are also RSGs but they will have been too faint for spectral typing and hence not been included in the work by Drout et al. (2012). Three of the variables in the top of the AGB branch may instead be massive AGB stars or super-AGB stars (Fig. 29).

5.3.5 The LBV Var C

Humphreys et al. (2014) identified a small number of LBVs in M33, one of which is called 'Var C'. Since its discovery, a series of eruptions have been witnessed in this star: 1940–1953 (Hubble & Sandage 1953); 1964–1970 (Rosino & Bianchini 1973); and 1982–1993 (Humphreys et al. 1988; Szeifert et al. 1996). By 1998, it had returned to a minimum state (Burggraf et al. 2014), but soon another, shorter episode of maximum light was seen from 2001 until 2005 (Viotti et al. 2006; Clark et al. 2012). Currently, it is in a hot quiescent stage (Humphreys et al. 2014).

Var C was detected in our WFCAM survey four, five and ten times in the J, H, and K-band, respectively. The photometry is reliable since there is no neighbouring star bright enough to seriously affect the photometry. The mean magnitudes are $\langle J \rangle = 16.32$ mag, $\langle H1 \rangle = 6.14$ mag, and $\langle K_s \rangle = 15.75$ mag; with $\langle J - K_s \rangle = 0.57$ mag, it is one of the bluer confirmed variable stars in our list. Over the two years of our monitoring campaign with WFCAM, Var C has steadily diminished its brightness, though in 2007 it seems to have stabilized (Fig. 30).

5.3.6 Spitzer mid-IR variability survey

Five epochs of *Spitzer* Space Telescope imagery in the 3.6-, 4.5- and 8-μm bands have been analysed by McQuinn et al. (2007), to identify variable stars using a similar method to that we used ourselves.

The *Spitzer* images covered nearly a square degree, slightly larger than our WFCAM survey; out of 40 571 *Spitzer* sources, 2868 stars fall outside the WFCAM monitoring coverage. Among the stars that *Spitzer* detected within the region in common with our survey, 36 411 are also in our photometric catalogue, down to a little below the RGB tip (Fig. 31). Hence, the recovery rate is ∼97 per cent. The recovery rate of the *Spitzer* survey for RSGs, bright AGB stars, and dusty AGB star variables from our WFCAM survey is good. Blending is only problematic for stars within the central square kpc of M33 (cf. Paper I), where the recovery rate decreases to ∼70 per cent.

Among the 2923 variable stars identified with *Spitzer*, 985 were identified as variable stars also in our WFCAM survey. This corresponds to a recovery rate of 35 per cent (excluding 113 stars that fall outside the WFCAM coverage), i.e. slightly higher than the recovery rate by the WFCAM survey of UIST variable stars in the central square kpc (cf. Section 3.1). On the other hand, 3661 of our WFCAM variable stars had not been identified as variable stars in the *Spitzer* survey. Both surveys do well in detecting variable dusty AGB stars; the WFCAM survey is also sensitive to fainter, less dusty variable red giants (Fig. 32) that were too faint for *Spitzer*.

Fig. 33 shows a mid-IR CMD, with a well-populated sequence off from which a branch extends towards redder colours and fainter 3.6-μm brightness starting around [3.6] ∼ 14–16 mag and

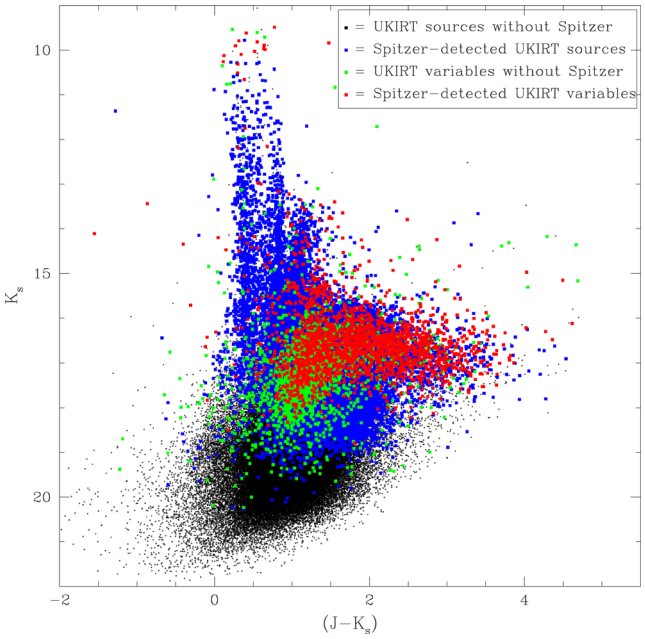

Figure 31. As Fig. 25, for the *Spitzer* mid-IR variability survey (McQuinn et al. 2007).

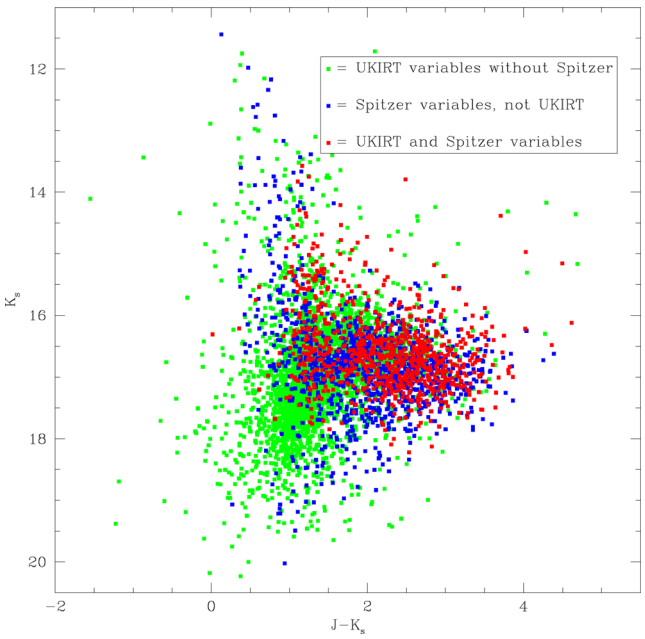

Figure 32. The variable stars that were or were not identified with WFCAM or *Spitzer*.

([3.6] − [4.5]) > 0.2 mag. This branch mostly comprises dust-enshrouded objects, with a high fraction of WFCAM variable stars. The WFCAM variables are plentiful also among the brighter 3.6-μm sources in the diagram; these are massive AGB stars and RSGs. The M-type stars form a sequence of increasing 3.6-μm brightness, with carbon stars located along part of this sequence. The near-absence of M-type or carbon stars in the red branch of dust-enshrouded objects is due to the limited sensitivity of the optical spectral typing survey. The Padova isochrones seem to underestimate the 3.6-μm brightness by a factor three or so, most notable in the missing of the 1-Gyr isochrone of the red branch.

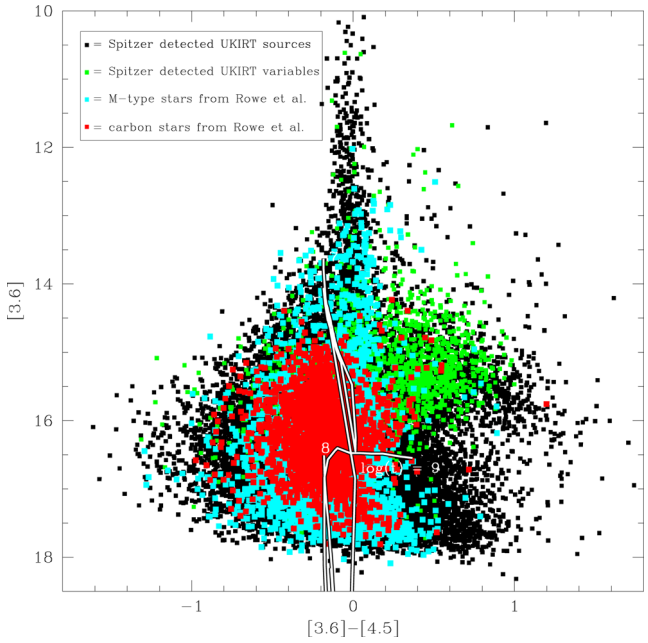

Figure 33. Mid-IR CMD of *Spitzer* photometry of our UKIRT/ WFCAM sources, with WFCAM variables highlighted in green and M-type and carbon stars from Rowe et al. (2005) in blue and red, respectively. Isochrones from Marigo et al. (2008) for 10 Myr, 100 Myr, and 1 Gyr are overlain for comparison.

5.3.7 *Sources variable at 24 μm*

Montiel et al. (2014) have identified 24 sources in M33 that are variable at a wavelength of 24 μm, based on *Spitzer* data with the MIPS instrument. One of these is NGC 604 (see below); the other sources could be dusty evolved stars.

We find that VC6, 8, 9, 13, 16, 21, and 23 (their nomenclature) are variable with high confidence and VC10, 17, and 20 probably (but with fewer near-IR epochs so less reliable). These are all red, with $(J - K_s) > 2.4$ mag (Fig. 34). We do not detect variability in VC14 but its photometry – $(J - K_s) = 0.94$ mag, $K_s = 13.32$ mag – is consistent with being a RSG and thus confirms the identification by Montiel et al. with the M2-type 760-d semiregular variable star VHK 71 (van den Bergh, Herbst & Kowal 1975); VC17 is likely variable and its photometry – $(J - K_s) = 3.5$ mag, $K_s = 14.87$ mag – is consistent with it being a dusty RSG.

On the other hand, for VC7 we only find a moderately red star without detected variability; this is probably the counterpart of the optical variable star with a 143-d period with which Montiel et al. associated VC7, but not of the 24-μm variable itself as the 10-μm absorption in the latter appears incompatible with such rapid variability.

None of the 24-μm variables with ([3.6] − [8.0]) > 4 mag – which includes all of their far-IR detections – were identified by us as near-IR variables. If this is because they are in fact not dusty evolved stars, then this would explain why they do not obey the evolved stars sequences in their [3.6]–[8.0] *versus* [3.6]–[4.5] diagram; they may instead be young stellar objects.

VC1 in Montiel et al. (2014) corresponds to NGC 604, the second largest extragalactic H II region in the Local Group (after 30 Doradus in the LMC). It is a young star-forming region with an age of 3–5 Myr (e.g. Wilson & Matthews 1995; Pellerin 2006). Located some 12 arcmin from the centre of M33, it spans around 4.1 pc with a core–halo structure (Melnick 1980). NGC 604 has been

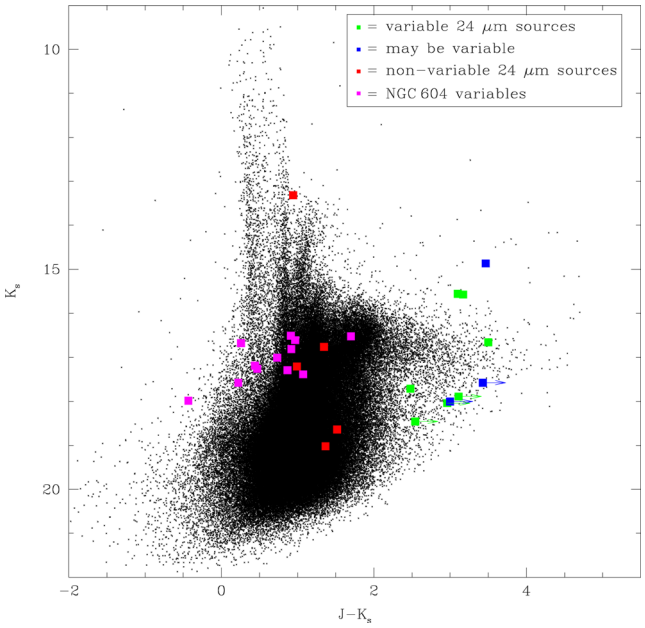

Figure 34. Near-IR CMD showing the 24-μm variables from Montiel et al. (2014) that were detected in our UKIRT/WFCAM survey. The variability indication refers to our near-IR survey.

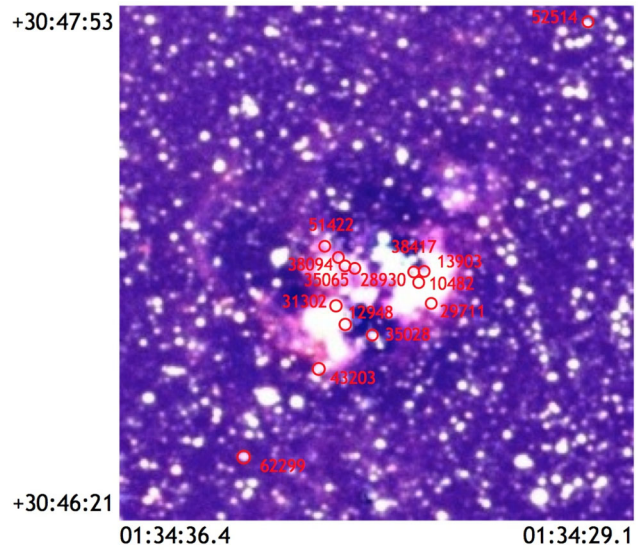

Figure 35. WFCAM JHK_s composite of the NGC 604 H II region in M33. The WFCAM variable stars are identified in red.

studied throughout the electromagnetic spectrum, including radio (Churchwell & Grass 1999; Tosaki et al. 2007), IR (Higdon et al. 2003), optical (Tenorio-Tagle et al. 2000), ultraviolet (Keel, Holberg & Treuthardt 2004), and X-ray (Maíz-Apellániz, Pérez & Mas-Hesse 2004). These studies were mostly concerned with the effect of the massive star formation on the surrounding ISM. Using WFCAM, we have identified 12 near-IR variable stars within NGC 604, which are shown in Fig. 35.

In the near-IR CMD (Fig. 34), the sources within NGC 604 are neither particularly luminous nor red – in fact, most have $(J - K_s) < 1$ mag. We suspect that this group of variables may include any or all of the following types of sources: (i) young early-type stars; (ii) stars whose photometry is affected by nearby stars and/or nebulosity; and (iii) a dusty carbon star not born in NGC 604 (at $(J - K_s) = 1.7$ mag).

6 CONCLUSIONS

WFCAM on UKIRT was used to extend our near-IR monitoring survey of the Local Group spiral galaxy M33, from the central square kpc to a square degree. *K*-band observations were complemented with occasional *J*- and *H*-band observations to provide colour information.

The photometric catalogue comprises 403 734 stars, among which 4643 stars display large-amplitude variability. Investigation of the light curves and location on the near-IR CMD with respect to theoretical models of stellar evolution indicate that most of these stars are AGB stars or RSGs. They are concentrated towards the centre of M33, more so than RGB stars. The majority of very dusty stars which are heavily reddened even at IR wavelengths are variable.

Cross-matching with optical monitoring campaigns and mid-IR variability searches conducted with *Spitzer*, shows that the UKIRT/WFCAM catalogue of variable stars is vastly more complete for the dusty variables than the optical surveys, and more complete for less dusty variables than the *Spitzer* surveys. Our catalogue is made publicly available at the CDS.

This work forms the basis for the next two papers in this series, to derive the SFH (Paper V) and to measure the rate and location of dust production (Paper VI) across M33.

ACKNOWLEDGEMENTS

We thank the staff at UKIRT for their excellent support of this programme, and the referee for her/his constructive report. JvL thanks the School of Astronomy at IPM, Tehran, for their hospitality during his visits. We are grateful for financial support by The Leverhulme Trust under grant no. RF/4/RFG/2007/0297, by the Royal Astronomical Society, and by the Royal Society under grant no. IE130487.

REFERENCES

Benjamin R. A. et al., 2005, ApJ, 630, L149
Bertelli G., Bressan A., Chiosi C., Fagotto F., Nasi E., 1994, A&AS, 106, 275
Bonanos A. Z. et al., 2006, ApJ, 652, 313
Burggraf B. et al., 2014, A&A, submitted
Churchwell E., Grass W. M., 1999, ApJ, 514, 188
Cioni M.-R. L. et al., 2008, A&A, 487, 131
Clark J. S., Castro N., Garcia M., Herrero A., Najarro F., Negueruela I., Ritchie B. W., Smith K. T., 2012, A&A, 541, A146
Deul E. R., van der Hulst J. M., 1987, A&AS, 67, 509
Drout M., Massey P., Meynet G., 2012, ApJ, 750, 97
Engargiola G., Plambeck R. L., Rosolowsky E., Blitz L., 2003, ApJ, 149, 343
Girardi L., Groenewegen M. A. T., Hatziminaoglou E., da Costa L., 2005, A&A, 436, 895
Girardi L., Marigo P., 2007, A&A, 462, 237
Gullieuszik M., Rejkuba M., Cioni M. R., Habing H. J., Held E. V., 2007, A&A, 475, 467
Hartman J. D., Bersier D., Stanek K. Z., Beaulieu J.-P., Kałużny J., Marquette J.-B., Stetson P. B., Schwarzenberg-Czerny A., 2006, MNRAS, 371, 1405
Higdon S. J. U., Higdon J. L., van der Hulst J. M., Stacey G. J., 2003, ApJ, 592, 161

Hodierna G. B., 1654, De Systemate Orbis Cometici, Deque Admirandis Coeli Characteribus (About the systematics of the cometary orbit, and about the admirable objects of the sky)
Hubble E., Sandage A., 1953, ApJ, 118, 353
Humphreys R. M., Leitherer C., Stahl O., Wolf B., Zickgraf F.-J., 1988, A&A, 203, 306
Humphreys R. M., Weis K., Davidson K., Bomanas D. J., Burggraf B., 2014, ApJ, 790, 48
Iben I., Jr, Renzini A., 1983, ARA&A, 21, 271
Javadi A., van Loon J. Th., Mirtorabi M. T., 2011a, MNRAS, 411, 263 (Paper I)
Javadi A., van Loon J. Th., Mirtorabi M. T., 2011b, MNRAS, 414, 3394 (Paper II)
Javadi A., van Loon J. Th., Mirtorabi M. T., 2011c, in Kerschbaum F., Lebzelter T., Wing R. F., eds, ASP Conf. Ser. Vol. 445, Why Galaxies Care About AGB Stars II: Shining Examples and Common Inhabitants. Astron. Soc. Pac., San Francisco, p. 497
Javadi A., van Loon J. Th., Khosroshahi H., Mirtorabi M. T., 2013, MNRAS, 432, 2824 (Paper III)
Keel W. C., Holberg J. B., Treuthardt P. M., 2004, AJ, 128, 211
Krisciunas K. et al., 1987, PASP, 99, 887
Levesque E. M., 2010, in Leitherer C., Bennett P., Morris P., van Loon J. Th., eds, ASP Conf. Ser. Vol. 425, Hot and Cool – Bridging Gaps in Massive Star Evolution. Astron. Soc. Pac., San Francisco, p. 103
Levesque E. M., Massey P., Olsen K. A. G., Plez B., Josselin E., Maeder A., Meynet G., 2005, ApJ, 628, 973
McQuinn K. B. W. et al., 2007, ApJ, 664, 850
Macri L. M., Stanek K. Z., Sasselov D. D., Krockenberger M., Kałużny J., 2001, AJ, 121, 861
Maíz-Apellániz J., Pérez E., Mas-Hesse J. M., 2004, AJ, 128, 1196
Marigo P., Girardi L., Bressan A., Groenewegen M. A. T., Silva L., Granato G. L., 2008, A&A, 482, 883
Massey P., Olsen K. A. G., Hodge P. W., Strong S. B., Jacoby G. H., Schlingman W., Smith R. C., 2006, AJ, 131, 2478
Melnick J., 1980, A&A, 86, 304
Messier C., 1771, Mem. Acad., 448
Mochejska B. J., Kałużny J., Stanek K. Z., Sasselov D. D., Szentgyorgyi A. H., 2001a, AJ, 121, 2032
Mochejska B. J., Kałużny J., Stanek K. Z., Sasselov D. D., Szentgyorgyi A. H., 2001b, AJ, 122, 2477
Montiel E. J., Srinivasan S., Clayton G. C., Engelbracht C. W., Johnson C. B., 2014, AJ, preprint (arXiv:1411.6008)
Pellerin A., 2006, AJ, 131, 849
Pierce M. J., Jurcević J. S., Crabtree D., 2000, MNRAS, 313, 271
Pietsch W., Misanovic Z., Haberl F., Hatzidimitriou D., Ehle M., Trinchieri G., 2004, A&A, 426, 11
Rosino L., Bianchini A., 1973, A&A, 22, 453
Rowe J. F., Richer H. B., Brewer J. P., Crabtree D. R., 2005, AJ, 129, 729
Sarajedini A., Barker M. K., Geisler D., Harding P., Schommer R., 2006, AJ, 132, 1361
Skrutskie M. F. et al., 2006, AJ, 131, 1163
Stetson P. B., 1987, PASP, 99, 191
Stetson P. B., 1993, in Butler C. J., Elliott I., eds, Proc. IAU Colloq. Vol. 136, Stellar Photometry – Current Techniques and Future Developments. Cambridge Univ. Press, Cambridge, p. 291
Stetson P. B., 1996, PASP, 108, 851
Szeifert T., Humphreys R. M., Davidson K., Jones T. J., Stahl O., Wolf B., Zickgraf F.-J., 1996, A&A, 314, 131
Tenorio-Tagle G., Muñoz-Tuñon C., Pérez E., Maíz-Apellániz J., Medina-Tanco G., 2000, ApJ, 541, 720
Thompson T. A., Prieto J. L., Stanek K. Z., Kistler M. D., Beacom J. F., Kochanek C. S., 2009, ApJ, 705, 1364
Tosaki T., Miura R., Sawada T., Kuno N., Nakanishi K., Kohno K., Okumura S. K., Kawabe R., 2007, ApJ, 664, L27
van den Bergh S., Herbst E., Kowal C. T., 1975, ApJS, 29, 303
van Loon J. Th., 2010, in Leitherer C., Bennett P., Morris P., van Loon J. Th., eds, ASP Conf. Ser. Vol. 425. Hot and Cool – Bridging Gaps in Massive Star Evolution. Astron. Soc. Pac. San Francisco, p. 279
van Loon J. Th., Zijlstra A. A., Whitelock P. A., Waters L. B. F. M., Loup C., Trams N. R., 1997, A&A, 325, 585
van Loon J. Th., Groenewegen M. A. T., de Koter A., Trams N. R., Waters L. B. F. M., Zijlstra A. A., Whitelock P. A., Loup C., 1999, A&A, 351, 559
van Loon J. Th., Cioni M.-R. L., Zijlstra A. A., Loup C., 2005, A&A, 438, 273
van Loon J. Th., van Leeuwen F., Smalley B., Smith A. W., Lyons N. A., McDonald I., Boyer M. L., 2007, MNRAS, 382, 1353
van Loon J. Th., Cohen M., Oliveira J. M., Matsuura M., McDonald I., Sloan G. C., Wood P. R., Zijlstra A. A., 2008, A&A, 487, 1055
Viotti R. F., Rossi C., Polcaro V. F., Montagni F., Gualandi R., Norci L., 2006, A&A, 458, 225
Whitelock P. A., Feast M. W., van Loon J. Th., Zijlstra A. A., 2003, MNRAS, 342, 86
Wilson C. D., Matthews B. C., 1995, ApJ, 455, 125
Wood P. R., 1998, A&A, 338, 592
Wood P. R., Whiteoak J. B., Hughes S. M. G., Bessell M. S., Gardner F. F., Hyland A. R., 1992, ApJ, 397, 552
Zaritsky D., Elston R., Hill J. M., 1989, AJ, 97, 97

This paper has been typeset from a TEX/LATEX file prepared by the author.